Title

CROSS SECTION MEASUREMENT FOR NON-STRANGE FINAL STATES AND SINGLE PION PRODUCTION IN +p INTERACTIONS AT 3.6 GeV/c

Author

Macnaughton, J.

Publication Date

1976-07-01

Submitted to Nuclear Physics B

LBL-5339
Preprint C. 1

CROSS SECTION MEASUREMENT FOR NON-STRANGE FINAL STATES AND SINGLE PION PRODUCTION IN $\pi^+ p$ INTERACTIONS AT 3.6 GeV/c

J. MacNaughton, W. R. Butler, D. G. Coyne, C. Fu, and G. H. Trilling

July 1976

Prepared for the U. S. Energy Research and Development Administration under Contract W-7405-ENG-48

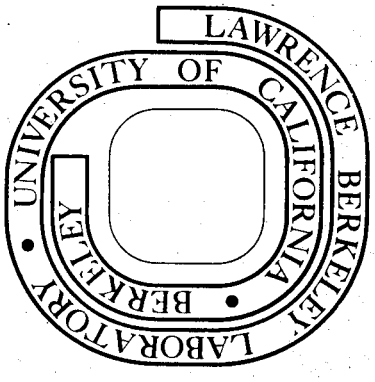

DISCLAIMER

LBL-5339

CROSS SECTION MEASUREMENT FOR NON-STRANGE FINAL STATES AND SINGLE PION PRODUCTION IN $\pi^+ p$ INTERACTIONS AT 3.6 GeV/c *)

J. MacNaughton
Institute for High Energy Physics of the Austrian Academy of Sciences, Vienna

W.R. Butler
Department of Physics, David Lipscomb College, Nashville, Tennessee

D.G. Coyne
Department of Physics, Princeton University, Princeton, New Jersey

C. Fu
Department of Physics, Illinois Institute of Technology, Chicago, Illinois

G.H. Trilling
Department of Physics and Lawrence Berkeley Laboratory, University of California, Berkeley, California

A B S T R A C T

Cross sections are presented for all final states without strange particle production. Contributions to single pion production are found from i) $\Delta(1238)\pi$ ii) $\rho^+ p$ iii) nucleon diffractive dissociation into $N\pi$ iv) $N^*(1688)\pi^+$ v) "phase space". Processes i), ii) and iii) are studied in some detail taking into account overlaps between the various subchannels.

---

*) Work was begun at Lawrence Berkeley Laboratory, supported in part by the Energy Research and Development Administration.

1. Introduction

Many experiments on $\pi^+ p$ interactions in hydrogen bubble chambers have been carried out in recent years. This technique provides the possibility to detect nearly all charged secondaries with rather accurate momentum and angular measurements. However gathering large statistics is cumbersome, thus new experiments continue to supply additional information. The present experiment provides a fairly accurate measurement of cross sections for channels without strange or neutral particles in the final state. The important channels in single pion production i) $\Delta(1238)\pi$, ii) $\rho^+ p$, iii) nucleon diffractive dissociation are studied with methods which allow for overlap between competing subchannels. The methods used are not as complicated as prism plot analysis [1] or analytical multidimensional multichannel analysis e.g. as proposed by Van Hove[2], but should not be as sensitive to reflections of competing channels as some more straightforward analysis methods. It is also found that $N^*(1688)\pi$ and "phase space" contribute to single pion production.

The experimental procedure is described in section 2, cross section determinations are given in section 3, and single pion production is analyzed in section 4. Section 4.1 describes the general features of single pion production, section 4.2 contains a discussion of problems with ambiguous events, section 4.3, 4.4 and 4.5 are concerned with the study of the subchannels $\pi^o \Delta^{++}$, nucleon diffractive dissociation and ρ^+ production respectively, section 4.6 describes $N^*(1688)$ production, and section 4.7 provides evidence for "phase space". The results are summarized in section 5.

2. Experimental Procedure

About 75,000 pictures were scanned for all interaction topologies. Events were predigitized and measured on the

LBL Flying-Spot Digitizer. If the first measurements were not satisfactory, both the predigitization and the FSD measurements were repeated. After two measurement failures, further remeasurements were made on Franckenstein measuring projectors using the COBWEB on-line computer-controlled system.

The results of FSD and Franckenstein measurements were analyzed by the kinematic fitting program SIOUX. The hypotheses included in the kinematic fitting, with the exception of topologies containing strange particle decays, are shown in Table 1. We have included the strange particle final state $\pi^+K^+K^-p$, because, though topologically identical to any four-prong event, it is readily distinguishable by kinematic fitting. We have also included the reaction $pp \rightarrow \pi^+\pi^-pp$ to obtain a measure of proton contamination in the incident beam.

The results of kinematic fitting for each event were examined in conjunction with track ionization information obtained from either the FSD output or visual inspection of the event. The following classes of hypotheses were discarded:

1) All hypotheses inconsistent with measured or visually estimated bubble densities.
2) All constrained fits for which the χ^2 was greater than the cutoff values of 24 for a four-constraint fit and 6.7 for a one-constraint fit.
3) All unconstrained fits for which the effective mass squared of neutral particles was too small to be consistent with at least two neutral hadrons of appropriate baryon number.

Having made the discards indicated, we treated the remaining hypotheses as follows:

a) All remaining four-constraint hypotheses were accepted.
b) If there were no four-constraint hypotheses for a given event, all one-constraint hypotheses were accepted.
c) If there were no constrained fits, all missing mass hypotheses were accepted.

If there were no acceptable hypotheses constrained or unconstrained for a given event, it was remeasured.

In addition to satisfying the kinematic fits as described above, events had to satisfy certain criteria of acceptability such as location within a given fiducial volume, having a proper incident beam track, being measurable on all three views, etc.

The beam had a non-negligible proton contamination. In order to monitor this contamination, the hypothesis $pp \rightarrow \pi^+\pi^-pp$ was attempted for all four-prong events. This four-constraint fit has the important feature that it is only rarely ambiguous with the corresponding four-constraint pion fit $\pi^+p \rightarrow \pi^+\pi^-\pi^+p$. To determine the effects of fitting incident protons as though they were pions, we took a small amount of film with the beam tuned to give protons. The procedure to correct for proton contamination was then a two-fold one of (i) selecting as our basic sample only those rolls in which the contamination, as measured by the number of unique $pp\pi^+\pi^-$ fits, was small and (ii) subtracting from any distributions obtained from these rolls corresponding distributions from the sample of film with pure or nearly pure incident proton beam normalized to the same number of $pp\pi^+\pi^-$ fits. For two-dimensional scatter plots, events from the incident π^+ sample which were closest neighbors to incident proton events were removed. The actual average proton contamination in the π^+ sample was 7 %. More details about the experimental procedure are given in ref.3.

3. Cross Section Determinations

3.1 Description of Procedure

Cross sections were obtained from a breakdown into the final states listed in Table 1 plus final states with strange particle signatures. Normalization was achieved by taking the total cross section to be the value obtained from counter

measurements at 3.63 GeV/c, namely 28.18 ± o.o15 mb. The total number of events involved was approximately 2o,ooo. The following types of corrections were considered:

(1) Scanning Efficiency

Since normalization is made to a fixed total cross section, only the differences in scanning efficiency between various topologies are of importance. The elastic scattering, which poses a special problem because of the inefficiency for detecting events with low momentum transfers, is discussed in a separate paper [4] and will not be considered further here. About 1o % of the film was rescanned to study scanning efficiency as a function of event type. Aside from forward elastic scatters, the single scan efficiencies were found to be about 98 % with no significant variation from one topology to another. An uncertainty of ± 2 % has been added to the errors in cross section to take account of any unobserved differential scanning inefficiency.

(2) Unresolved Events

Approximately 7 % of the events were unresolved after three measurement attempts either because of geometrical reconstruction failure or because no acceptable constrained or missing mass hypothesis was found. The latter category involves principally events which should have satisfied a four-constraint fit but which because of measurement errors fell outside the χ^2 cutoff limits specified earlier. Inspection of the event and the measurement output were generally adequate for identifying the four-constraint events on the tail of the χ^2 distribution. Events which failed geometrical reconstruction were distributed among the various reactions corresponding to the given topology in proportion to the accepted numbers of events.

(3) Fit Ambiguities

Ambiguities between fits of a different constraint class were, as discussed earlier, resolved in favor of the higher constraint class. Ambiguities between fits of the same constraint class were relatively more prevalent among events with a neutron in

the final state than with a proton because of the unavailability of ionization information for the usually peripheral baryon. Thus extreme limits on the distribution of ambiguous events can be set by (i) assuming all ambiguous events have an outgoing neutron, (ii) assuming ambiguous events should be distributed in the same proportion as unambiguous events. The cross section for each channel was determined from the number of unambiguous events plus the number of ambiguous events halfway between these two extremes. To take account of the uncertainty introduced by this procedure an error equal to half the difference between the two extreme situations was folded in. Accurate measurements for the cross sections of final states with neutral particles await experiments with some means of detecting neutral particles.

3.2 Results

The results of the cross section determinations are given in Table 2. The total strange particle cross section which included states with and without strange particle signature comes from the study of W.R. Butler et al.[5] using a much larger sample of film from the same experiment. It is interesting to note one general statement which can be made from the results in Table 2: for events with a given number of pions in the final state, those topologies which minimize the number of pions in any one charge state are favored. Thus

$$\sigma(p\pi^+\pi^0) > \sigma(n\pi^+\pi^+)$$

$$\sigma(p\pi^+\pi^+\pi^-\pi^0) > \sigma(n\pi^+\pi^+\pi^+\pi^-)$$

$$\sigma(p\pi^+\pi^+\pi^+\pi^-\pi^-\pi^0) > \sigma(n\pi^+\pi^+\pi^+\pi^+\pi^-\pi^-)$$

Also included in Table 2 are cross sections for the final states $\rho^+ p$, $\Delta\pi$, $N^*(1688)\pi$, and proton diffractive dissociation, determined as discussed below.

4. Study of single pion production

4.1 General features

The reactions studied are:

$$\pi^+ p \rightarrow \pi^+ p \pi^0 \qquad (1)$$

$$\pi^+ p \rightarrow \pi^+ \pi^+ n \qquad (2)$$

The analysis is based on a sample of 4717 events for reaction (1) and 3115 events for reaction (2). These events include about 1099 events produced by proton contamination which are subtracted out as described in section 2.

The Dalitz plots for reactions (1) and (2) are shown in Fig.1 and Fig.2 respectively. The major features of Fig.1 include production of the ρ^+ and Δ^{++} and a broad enhancement in the region of low $p\pi^0$ invariant mass. Similarly the population density of Fig.2 shows a marked increase in the neighborhood of low $n\pi^+$ mass.

The extremely peripheral nature of these dominating features is shown in the Chew-Low plots of Fig.3a,b,c and Fig.4a,b, for reactions (1) and (2) respectively.

The major processes which dominate single pion production can then be summarized as follows:

$$\pi^+ p \rightarrow \pi^0 \Delta^{++} \qquad (3a)$$

$$\rightarrow \rho^+ p \qquad (3b)$$

$$\rightarrow \pi^+ (\pi^0 p) \qquad (3c)$$

$$\rightarrow \pi^+ (\pi^+ n) \qquad (3d)$$

where (3c) and (3d) are used to denote the production of broad and highly peripheral $p\pi^0$ and $n\pi^+$ enhancements which we shall associate with diffractive dissociation of the proton target.

4.2 Problems with ambiguous events

Due to the peripherality of the production of the above channels, (3a), (3b), (3c) give rise predominantly to a slow proton in the laboratory. If $|t_p| \lesssim 1.2$ (GeV/c)^2 - corresponding to a laboratory momentum of about 1.27 GeV/c -, the proton can almost always be identified uniquely by ionization estimates. This is satisfied for almost all events for (3a) (3b) (3c) in kinematic regions where the production cross section is large enough to be studied in this experiment. This is not true for (3d), giving large to a sizeable ambiguity rate here. (3d) has not been used in this analysis except for the isospin decomposition, where it is hoped that the introduced biases are small due to the large diffractive cross section in the region studied. The similarities between (3c) and (3d) give added confidence here.

4.3 The Process $\pi^+ p \to \pi^o \Delta^{++}$

This process has been investigated previously many times. A partial list of experimental studies is given in ref.6 and theoretical studies in ref.7.

Fig.5 shows the $p\pi^+$ mass distribution for the channel $p\pi^+\pi^o$. Besides a prominent Δ^{++} peak, the histogram indicates a distribution which differs from phase space in that there is a considerable excess of events at high mass. Inspection of Fig.1 shows that this excess is largely a reflection of the broad low mass $p\pi^o$ enhancement although there also appears to be some contribution from the $\Delta^{++}(1950)$.

In order to determine the cross section we made a fit to the histogram of Fig.5 for $m(p\pi^+) \lesssim 1.75$ GeV with an incoherent superposition of Δ^{++} and a background of the form

$$\text{background} = \text{phase space} \times \left[1 + b m^2(p\pi^+)\right] \qquad (4)$$

A satisfactory fit with $b = 0.2 \, ^{+0.3}_{-0.2}$ GeV^{-2} was obtained, leading to a cross section of 0.43 ± 0.03 mb for this reaction. This value agrees with a recent compilation by Bloodworth et al.[6] Using appropriate Clebsch-Gordan coefficients, one easily finds that total $\pi\Delta$ contribution to single pion production in $\pi^+ p$ collisions at our momentum is 0.72 ± 0.05 mb.

In determining the differential cross section for Δ production, the following procedures were used to minimize the effects of background:

(i) For $-t_{\pi^0} < 0.4$ (GeV/c)^2 only the backward region of $\cos\alpha$, $-1 < \cos\alpha < 0$ was used in order to minimize the effects of the ρ-Δ overlap region. Here α is the $p\,\pi^+$ decay angle in the Jackson frame.

(ii) The Δ populations in each momentum transfer bin were determined by fitting the corresponding $m(p\,\pi^+)$ spectra to a superposition of Δ^{++} and phase space.

The resulting $d\sigma/dt$ distribution is shown in Fig.6. The most striking feature is the large dip at -0.5 (GeV/c)^2. Although other experiments have previously exhibited this dip, most have not indicated as deep a drop, consistent in fact with zero population at that value of t_{π^0}, as the present data. Actually careful inspection of Fig.3a shows very clearly the absence of any signal above background near -0.5 (GeV/c)^2 followed at higher momentum transfers with a considerable population. Above 2 (GeV/c)^2 there appears to be at best very little Δ contribution.

The shape of $d\sigma/dt$ with its dip at -0.5 (GeV/c)^2 has been interpreted in terms of simple Regge theory as arising from a nonsense-unphysical signature zero in the helicity flip amplitude. Since the basic behavior appears dominated by this helicity flip amplitude, the dip should actually be a zero in the cross section. The experimental result shown in Fig.6 strongly supports this prediction unlike most previous experiments which showed only a slight dip or shoulder. Indeed the theoretical curve of Maor and Krammer[7], based on a Reggeized

ρ exchange model, gives an excellent representation of our data while being only a fair fit to the actual experiments from which the parameters were derived.

The density matrix elements for process(3a), shown in Fig.7, were obtained using a $p\pi^+$ mass band between 1.12 and 1.32 GeV, but again considering only backward $\cos\alpha$ to minimize interference problems with the ρ . Unfortunately the statistical accuracy is not very great, but within this accuracy there is fair agreement with the predictions of the Stodolsky-Sakurai M1 model, $\rho_{33} = 0.375$, $\mathrm{Re}\,\rho_{3-1} = 0.22$, $\mathrm{Re}\rho_{31} = 0$.

4.4 Diffractive Dissociation of the Proton

In Fig.3b and 4a there is a large excess of events at small momentum transfer and fairly low mass. The enhancement certainly includes some Δ^+ production, but is far too broad and contains too many events to be explained entirely by Δ^+ production. The natural interpretation is in terms of diffractive dissociation of the nucleon, as represented schematically in terms of Pomeron exchange by the diagram of Fig.8. Since a diffractive process must preserve the isotopic spin, it is natural to analyze it by considering the isospin-1/2 combination

$$N_{1/2} = N(p\pi^0) + N(n\pi^+) - \frac{2}{3} N(p\pi^+)$$

where $N(N\pi)$ represents the population for a given $N\pi$ mass interval. We have imposed on the isospin-1/2 $N\pi$ mass spectrum so obtained one additional restriction: the cosine of the angle between the two outgoing pions in the center of mass of the $N\pi$ system under study is limited to the range 0.5 to -1 to eliminate background from ρ^+ production. The resulting isospin-1/2 spectrum is shown in Fig.9 for two momentum transfer intervals, $-t < 0.4$ $(\mathrm{GeV/c})^2$ and $-t < 0.1$ $(\mathrm{GeV/c})^2$. For the larger momentum transfer region a large, broad enhancement for the $N\pi$ mass region below 1.8 GeV is seen. The smaller momentum transfer cut narrows the $N\pi$ enhancement significantly. In Figs.10-12 the actual momentum transfer distributions for three different ranges of $N\pi$ mass, namely 1.08 - 1.3 GeV,

1.3 - 1.5 GeV, and 1.5 - 1.8 GeV, are shown. The slopes of the momentum transfer distributions clearly become flatter as the N π mass is increased. All these results are very similar to ones previously reported by Boesebeck et al.[8] for 8 and 16 GeV π^+p interactions and by Evans et al.[9] for 11.7 GeV/c π^+p interactions, and by Berlad et al.[10] for 3.9 GeV/c $\pi^\pm$p interactions. A rough estimate of the total cross section for the nucleon diffractive dissociation process is about 1.3 mb, or roughly 15 % of the elastic scattering cross section.

In summary:

i) The mass spectrum for $-t_{\pi^+} \lesssim 0.4$ (GeV/c)^2 extends from 1.1 GeV to 1.8 GeV at which point it drops off rapidly. There is no clearly established structure in the mass spectrum. In particular there is no evidence for a peak near 1688 MeV.

ii) For $-t_{\pi^+} \lesssim 0.1$ (GeV/c)^2 the N π mass spectrum is pushed much more toward low masses. This result is consistent with the observation that the t_{π^+} distribution drops off more sharply at low N π masses than at high ones. In agreement with the results of Boesebeck et al.[8] is the presence of a large population near 1.2 - 1.3 GeV, very much below the lowest mass isospin 1/2 resonance established in nucleon-pion phase shift analysis.

A further analysis of diffractive dissociation at this energy is difficult. In addition to possible large non-asymptotic contributions to the (p π^0) system itself, the effects of competing channels cannot be dealt with in the same manner as is done for Δ^{++} production (section 4.3) or ρ^+ production (section 4.5), since the primary method used in these sections for selecting out the amount of resonance production in each kinematic region is to fit mass spectra to a Breit-Wigner (rather narrow) + background (contains rather broad reflections from competing channels). This technique does not work for diffractive dissociation, since its mass spectrum is so broad.

4.5 Study of the $\rho^+ p$ Final State

4.5.1 Introduction

The study of ρ^+ production is complicated by background problems. It is useful to obtain some feeling for these problems by examining scatter plots of t'_p, the squared four-momentum transfer from incident to outgoing proton minus the kinematical minimum versus the $\pi^+\pi^0$ mass squared, for various regions of $\cos\alpha$ where α is the angle between incident and outgoing π^+ in the $\pi - \pi$ center of mass. These plots are shown in Fig.13a-e and 14a-e for ten bands of $\cos\alpha$, each of width 0.2. Evidently there is considerable ρ^+ production for all values of $\cos\alpha$. It is of particular interest to note the large background near the ρ both near $\cos\alpha = +1$ and near $\cos\alpha = -1$. These arise from the diffractive dissociation (reaction 3c) and from the Δ^{++} production (reaction 3a) respectively. It is also noteworthy that in the neighborhood of $\cos\alpha = 0$ there is practically nothing except ρ for low momentum transfers.

The almost complete absence of background near $\cos\alpha = 0$ has motivated us to examine the ρ parameters in that region. We have chosen as our data sample all events with $|\cos\alpha| < 0.5$. The background was parametrized as

$$\text{background} = \sum_{k=0}^{c} a_k m^k \times \text{phase space} \qquad (5)$$

where m is the $\pi - \pi$ mass and a_k are coefficients determined by the fit. Using a P-wave relativistic Breit-Wigner for the ρ^+ and fitting from 0.28 to 1.60 GeV we tried various values of the cutoff factor c. A reasonably good fit was obtained over this large mass range with $c = 2$, the χ^2 being 28 for 21 degrees of freedom. The data and fitted curve are shown in Fig.15, and the resulting parameters are $m_\rho = 765 \pm 8$ MeV and $\Gamma_\rho = 170 \pm 30$ MeV. The effect of measurement resolution on Γ_ρ is not significant.

4.5.2 Differential and Total Cross Sections

To separate ρ^+ from background, the following procedure was adopted. The data was divided into various regions of t'_p. For each region the $\pi - \pi$ mass spectrum was fit with an incoherent superposition of a background of the form (5) plus a P-wave Breit-Wigner having the fixed parameters m_ρ = 765 MeV, Γ_ρ = 170 MeV as determined above. At low momentum transfers it has been shown elsewhere that ρ production and diffractive dissociation interfere [11] hence for $-t'_p < 0.6$ (GeV/c)^2 only events with $\cos\alpha < 0$ were used, and the ρ intensity obtained thereby was doubled. At higher momentum transfers all events were used. This fitting procedure works much better for a t'_p distribution than for a t_p distribution because t'_p cuts distort the background much less than t_p cuts. This is of some importance in obtaining a background which varies much more slowly with $\pi - \pi$ mass than the ρ resonance. The resulting distribution $d\sigma/dt'$ for the ρ is shown in Fig.16. There is a sharp drop at very low momentum transfers with a dip about 0.5 (GeV/c)^2 followed by a secondary maximum near 0.8 (GeV/c)^2. Another minimum near 3 (GeV/c)^2 is finally followed by a slight rise in the backward direction. To give some idea of the significance of the data points for $-t'_p$ above 2 (GeV/c)^2 we exhibit in Fig.17 and Fig.18 the $\pi - \pi$ mass distributions for $2 < -t'_p < 4$ (GeV/c)^2 and $-t'_p > 4$ (GeV/c)^2 respectively. The dashed lines show the background and the solid lines the fitted curves. The principal features seen in the $d\sigma/dt'$ distribution including the secondary peak near 0.8 (GeV/c)^2 and the backward peak are evident just from inspection of the Chew-Low plot, Fig.3c. Thus although different procedures could lead to slight changes in $d\sigma/dt'$, the basic features appear to be independent of any particular fitting procedure. The total $\rho^+ p$ cross section is 0.80 $\pm$ 0.06 mb.

The dip in $d\sigma/dt'$ at $-t' = 0.5$ (GeV/c)^2 which, as will be shown later, is most likely associated with ω exchange has been reported in some studies of the reactions $\pi^\pm p \to \rho^\pm p$ and not

in others. Thus clear evidence for a dip is seen by Baton et al.[12], Michael and Gidal [12] and Williamson et al.[12]. Such structure finds a natural interpretation either in terms of a nonsense unphysical signature zero for ω exchange or in terms of the dual absorptive model of Harari [13].

4.5.3 Spin Density Matrix Elements

A very similar procedure to that used for the determination of $d\sigma/dt'$ was used to calculate ρ spin density matrix elements with appropriate background removed. For each matrix element the data were divided into two appropriate angular regions and the $\pi\pi$ mass spectrum for each region was fit to ρ and background as described earlier.

The results for various intervals of t' are shown as solid crosses in Fig.19 (Jackson frame) and Fig.2o (Helicity frame). The dashed crosses in Fig.19 and 2o are the values obtained by defining the rho as events with $o.66 < m_{\pi\pi} < o.86$ GeV. Obviously some sizeable differences are seen. This is not surprising since, as can be seen from Figs.13 - 14, even at relatively small $|t'|$, reflections from the competing channels - Δ^{++} production and diffractive dissociation - are important and give rise to reflections which are very anisotropic in the $\pi - \pi$ system decay angles. With t' cuts these reflections tend to be rather broad in $\pi\pi$ mass spectra, and their effects are largely removed by the fitting procedure. If t cuts are applied instead, these reflections into the $\pi\pi$ mass spectra tend to show more structure and are not so easily removed by the fitting procedure. To demonstrate the presence of reflections even at quite small t', a Dalitz plot for the $p\pi^+\pi^o$ final state with $-t'_p < o.o8$ $(GeV/c)^2$ is shown in Fig.21. In addition to a prominent ρ^+ band, Δ^{++} and diffractive dissociation bands are clearly visible. General background appears small.

To give an example showing how the differences between the solid and dashed crosses in Figs.19 and 2o arise, we show in Figs.22 and 23 typical $\pi\pi$ mass spectra for two appropriate angular intervals - those used for measuring ρ_{1-1} in the Jackson frame. The t' interval selected was $o.o8 < -t' < .5$ $(GeV/c)^2$. The appropriate angular intervals were $-1 < \cos\alpha < 0$ with $45^o < \phi < 135^o$

or $225^{\circ} < \phi < 315^{\circ}$ and $-1 < \cos\alpha < 0$ with $0^{\circ} < \phi < 45^{\circ}$ or $135^{\circ} < \phi < 225^{\circ}$ or $315^{\circ} < \phi < 360^{\circ}$ where ϕ is the Treiman-Yang angle. The solid curves in Figs.22 and 23 are the fits; the dashed lines are the background contributions. The solid cross in Fig.19 in the appropriate t' interval is calculated from the fitted numbers of rho events (difference between solid and dashed curves) (Figs.22, 23); whereas the corresponding dashed cross is calculated from the total numbers of events with $0.66 < m_{\pi\pi} < 0.86$ (Figs.22, 23).

The background is much larger in Fig.23 than Fig.22; this effect is due to the reflection of Δ^{++} production (process (3a)). If the region $\cos\alpha \lesssim 0$ had been included also in Fig.22 and Fig.23, the reflection of proton diffractive dissociation (process 3c) would also have caused a similar effect. Thus our result is that (except at very small t') ρ_{1-1} for ρ^{+} production is positive indicating that the ϕ distribution shows the two peak structure characteristic of a vector exchange contribution. The valleys between the peaks can be somewhat filled in by reflections of competing channels if insufficient care is taken in allowing for their effects.

The matrix elements of Fig.19 show a behavior characteristic of pion exchange only at very small momentum transfers ($-t' < 0.1$ (GeV/c)^2). In particular the matrix element ρ_{00} drops very rapidly with increasing $|t'|$. It is perhaps worth pointing out that a procedure of simply selecting a $\pi\pi$ mass band and calculating matrix elements as though the population within the band were pure ρ would lead to results whose variation with t' would be considerably less rapid (dashed crosses, Fig.19). The density matrix elements in Fig.19 are quite similar to those seen by Seidl [14] for the reaction $K^{+}p \to K^{*}p$ at 4.27 GeV/c. The rapid drop in ρ_{00} seen in Fig.19 is not seen by Haber et al.[15] using the prism plot analysis technique in $\pi^{+}p \to \rho^{+}p$ at 3.9 GeV. The prism plot analysis does not take interference between ρ^{+} and diffraction into account, but the value of the interference

phase found in ref.11 indicates that this is not the source of the discrepancy. A search (described in ref.3) was made for interference between Δ^{++} and ρ^{+} production. Little evidence for interference was found within the framework of the simple parametrization used, so this also does not seem to be the source of the discrepancy.

To study production mechanisms in a little more detail we have plotted in Fig.24 the cross sections $\rho_{00} d\sigma/dt'$, $(\rho_{11}+\rho_{1-1}) d\sigma/dt'$ and $(\rho_{11}-\rho_{1-1}) d\sigma/dt'$ (Jackson frame) which correspond to unnatural parity leading to helicity zero, natural parity and unnatural parity exchange leading to helicity one respectively. Both of the unnatural parity exchange cross sections (Figs.24a and c have the same shape within statistics, with the helicity zero state dominating by about a factor of 3. There is no significant contribution within our fairly large errors above $-t' \approx 0.4$ $(GeV/c)^2$. On the other hand the natural parity exchange provides essentially the entire contribution in the t region above $-t' \approx 0.8$ GeV $(\rho_{11}+\rho_{1-1} \approx 0.8)$. In agreement with ref.15, within our large errors, we see no evidence for a dip in $(\rho_{11}+\rho_{1-1}) d\sigma/dt'$ near $-t' = 0.5$ $(GeV/c)^2$, expected for ω exchange. A clear dip is seen by W. Michael and G. Gidal [12] and by Williamson et al. [12] who have better statistics.

4.6 Production of N*(1688)

Figures 25 a and b show the $n\pi^+$ and $p\pi^0$ mass spectra for the $n\pi^+\pi^+$ and $p\pi^+\pi^0$ reactions. The shaded events are for $|t_{\pi^+}| \geq 0.5$ $(GeV/c)^2$. There is clear evidence for production of N*(1688) at large momentum transfers. This effect has already been reported by Schotanus et al.[6] at 5 GeV/c and Bastien et al.[16] at 3.9 GeV/c. The cross section for N*(1688) production in these reactions is about 100 μb. In ref.6) and 16) a backward peak is seen for N*(1688) production; whereas inspection of Figs.3b and 4a indicates that in this experiment N*(1688) seems to be produced in a broad range of momentum transfer.

4.7 Possible "phase space" background

Inspection of Fig.3c shows that in addition to the ρ^+, the $\pi^+\pi^o$ system has peripheral contributions extending broadly to masses up to 1600 MeV which can be interpreted as reflections of both Δ^{++} production and proton diffractive dissociation into $p\pi^o$. To demonstrate this we show in Fig.26 a $\pi\pi$ system Chew-Low plot with events with $1.16 < m_{p\pi^+} < 1.3$ GeV and $-t_{\pi^o} < 0.4$ (GeV/c)^2 and $m_{p\pi^o} < 1.7$ GeV and $-t_{\pi^+} < 0.4$ (GeV/c)^2 removed. In Fig.26 this general enhancement at low $|t_p|$ has disappeared leaving only the ρ predominantly associated with low $|t_p|$. Similarly in Fig.4b one sees a general peripheral enhancement at small $|t_n|$ extending over all $\pi^+\pi^+$ masses. This is at least partially associated with proton diffractive dissociation into $n\pi^+$.

In Fig.26 in addition to the peripheral rho production (and a small backward rho production) there is a general background which appears to be nearly isotropic in t. This could be construed as evidence for a "phase-space"-like background. In particular it would be interesting to measure the energy dependence of the cross section for this effect. Care must be taken since events with $-t_p \lesssim 1.2$ (GeV/c)^2 play a large role in this realm, and as discussed in section 4.2, ambiguous events occur frequently in this region. Thus the observed number of events should rather be considered an upper limit on real $p\pi^+\pi^o$ events. It would be hoped that more accurate results could be obtained with a good detection efficiency for gamma rays resulting from π^o decays e.g. by using a track sensitive target.

5. Discussion

We find the following contributions to the $p\pi^+\pi^o$ final state:

i) $\Delta(1237)\pi$
ii) $\rho^+ p$
iii) proton diffractive dissociation
iv) $N^*(1688)\pi$
v) "Phase space"
vi) some evidence for $\Delta(1950)\pi$

Despite the large number of similar experiments carried out in recent years, some points remain to be settled such as the detailed shape of t distributions for resonance production near the dip regions and the t dependence of the spin density matrix elements (especially near the dips in the t dependence). It is clear that improvements here require experiments with more statistics and also better understanding of background problems, including disentanglement of the various reaction channels contributing to the final state. To solve the latter problem prism plot analysis [1] and the analytical multi-dimensional multi-channel analysis method of Van Hove[2] have been proposed. Only the latter method is suitable for study of interference between the various channels, e.g. between ρ^+ production and proton diffractive dissociation.[11] It should also be borne in mind that, contrary to the assumptions of ref.1 and ref.2, the various channels may be at least partially dual, further complicating the question of what should be considered as background in the study of a particular resonance.

Acknowledgements

We much appreciate the support of our scanning and measuring staff during the long years of this experiment, of the programming staff, especially Emmett Burns, who, among other responsibilities, adapted the SIOUX program to this experiment, of the Bevatron and 72'' bubble chamber crews during exposure of the film, and of the F.S.D. group under Howard White. We wish to thank Professors G. Goldhaber and K.W.J. Barnham for many helpful discussions.

References

1) J.E. Brau et al., Phys.Rev.Letters 27 (1971) 1481

2) L. Van Hove, IVth Int. Symposium on Multi-Particle Hadrodynamics, Pavia, 1973 ;
L. Van Hove, Topical Conference on Multi-Dimensional Analysis of Hadron Collisions, CERN 1974

3) J. MacNaughton, Ph.D. thesis, UCRL-2o178 (unpublished)

4) J. MacNaughton, W.R. Butler, D.G. Coyne, G.M. Hicks, G.H. Trilling, Nuclear Physics B33 (1971) 1o1

5) W.R. Butler, D.G. Coyne, G. Goldhaber, J. MacNaughton and G.H. Trilling, Phys.Rev.D7 (1973) 3177

6) M. Aderholz et al., Nuclear Physics B8 (1968) 45,
J. Bartsch et al., Phys.Letters 1o (1964) 229,
I.J. Bloodworth et al., Nuclear Physics B81 (1974) 231,
M. Deutschmann et al., Nuclear Physics B85 (1975) 31,
D. Evans et al., Nuovo Cimento 16A (1973) 299
G. Gidal et al., Phys.Rev.Letters 23 (1969) 994,
B. Haber et al., Phys.Rev.D11 (1975) 495,
J. H. Scharenguivel et al., Nuclear Physics B36 (1972) 363,
D. J. Schotanus et al., Nuclear Physics B22 (197o) 45

7) I.J. Bloodworth, Nuclear Physics B8o (1974) 23o,
P. Butera et al., Nuclear Physics B31 (1971) 455,
J.P. de Brion and C. Lewin, Nuovo Cimento 19A (1974) 225,
J.P. de Brion and R. Peschanski, Nuclear Physics B81 (1974) 484,
P. Gizbert-Studnicki, Acta Phys.Pol.B1 (197o) 235,
M. Krammer and U. Maor, Nuclear Physics B13 (1969) 651,
R. D. Mathews, Nuclear Physics B11 (1969) 339

8) K. Boesebeck et al., Nuclear Physics B28 (1971) 381

9) D. Evans et al., Nuovo Cimento 23A (1974) 291

10) G. Berlad et al., Nuclear Physics B75 (1974) 93

11) J. MacNaughton, W.R. Butler, D.G. Coyne, C. Fu and G.H. Trilling, UCRL-20833 (1971),
W. Michael, Phys.Rev.D7 (1973) 1985
J. MacNaughton et al., Nuclear Physics B, to be published

12) J.P. Baton and G. Laurens, Nuclear Physics B21 (1970) 551
W. Michael and G. Gidal, Phys.Rev. Letters 28 (1972), 1475
Y. Williamson et al., Phys.Rev.Letters 29 (1972) 1353

13) H. Harari, Phys.Rev.Letters 26 (1971), 1400

14) A. Seidl, Phys.Rev.D7 (1973) 621

15) B. Haber et al., Phys.Rev.D10 (1974) 1387

16) P.L. Bastien et al., Phys.Rev.D3 (1971) 2047

Table 1. Hypothesis list
for the kinematic fitting program for events without strange particle signature

Two-Prong	No. of Constraints
$\pi^+ p \rightarrow \pi^+ p$	4
$\rightarrow \pi^+ \pi^o p$	1
$\rightarrow \pi^+ \pi^+ n$	1
$\rightarrow \pi^+ p$ + missing mass	0
$\rightarrow \pi^+ \pi^+$ + missing mass	0
Four-Prong	
$\pi^+ p \rightarrow \pi^+ \pi^+ \pi^- p$	4
$\rightarrow \pi^+ K^+ K^- p$	4
$pp \rightarrow \pi^+ \pi^- pp$	4
$\pi^+ p \rightarrow \pi^+ \pi^+ \pi^- \pi^o p$	1
$\rightarrow \pi^+ \pi^+ \pi^+ \pi^- n$	1
$\rightarrow \pi^+ \pi^+ \pi^- p$ + missing mass	0
$\rightarrow \pi^+ \pi^+ \pi^+ \pi^-$ + missing mass	0
Six-Prong	
$\pi^+ p \rightarrow \pi^+ \pi^+ \pi^+ \pi^- \pi^- p$	4
$\rightarrow \pi^+ \pi^+ \pi^+ \pi^- \pi^- \pi^o p$	1
$\rightarrow \pi^+ \pi^+ \pi^+ \pi^+ \pi^- \pi^- n$	1
$\rightarrow \pi^+ \pi^+ \pi^+ \pi^- \pi^- p$ + missing mass	0
$\rightarrow \pi^+ \pi^+ \pi^+ \pi^+ \pi^- \pi^-$ + missing mass	0

Table 2) Cross sections.

Final state	Cross section (mb)	
Momentum	3.56 GeV/c	3.67 GeV/c
$p\pi^+$	6.93±0.23	7.15±0.21
$p\pi^+\pi^+\pi^-$	3.59±0.14	3.47±0.12
$p\pi^+\pi^+\pi^+\pi^-\pi^-$	0.20±0.02	0.22±0.02
$p\pi^+\pi^o$	2.51±0.2	2.36±0.2
$n\pi^+\pi^+$	1.50±0.2	1.68±0.3
$p\pi^+\pi^+\pi^-\pi^o$	3.22±0.1	3.32±0.1
$n\pi^+\pi^+\pi^-\pi^+$	0.55±0.03	0.57±0.04
$p\pi^+\pi^+\pi^-\pi^+\pi^-\pi^o$	0.17±0.02	0.165±0.02
$n\pi^+\pi^+\pi^+\pi^+\pi^-\pi^-$	0.016±0.03	0.017±0.03
$p\pi^+$MM	3.68±0.65	3.76±0.7
$\pi^+\pi^+$MM	2.76±1.2	2.50±1.3
$p\pi^+\pi^+\pi^-$MM	1.13±0.07	0.99±0.1
$\pi^+\pi^+\pi^+\pi^-$MM	0.51±0.07	0.52±0.1
$p\pi^+\pi^+\pi^-\pi^-\pi^+$MM	0.016±0.007	0.019±0.006
$\pi^+\pi^+\pi^+\pi^+\pi^-\pi^-$MM	0.003	0.001
Momentum	3.6 GeV/c	
$\pi^o\,\Delta^{++}$	0.43±0.03	
$\pi\,\Delta$	0.72±0.05	
$\rho^+ p$	0.80±0.06	
$N^*(1688)$	0.1	
proton diffractive dissociation	1.3	
total strange particle*) production[5]	1.3	

*) includes states with and without strange particle signature

Figure Captions

Fig.1 Dalitz plot for the final state $p\pi^+\pi^0$

Fig.2 Dalitz plot for the final state $n\pi^+\pi^+$

Fig.3 Scatter plot of momentum transfer squared vs. effective mass squared for a) $p\pi^+$, b) $p\pi^0$, c) $\pi^+\pi^0$ systems for the final state $p\pi^+\pi^0$

Fig.4 Scatter plot of momentum transfer squared vs. effective mass squared for a) $n\pi^+$, b) $\pi^+\pi^+$ systems for the final state $n\pi^+\pi^+$

Fig.5 $p\pi^+$ mass spectrum

Fig.6 $d\sigma/dt$ distribution for the final state $\Delta^{++}\pi^0$

Fig.7 t-dependence of spin density matrix elements for Δ^{++} decay in the final state $\Delta^{++}\pi^0$. Only events with $\cos\alpha < 0$ are used.

Fig.8 Diagram for proton diffractive dissociation with Pomeron exchange.

Fig.9 Mass distribution of the isospin 1/2 component of the $N\pi$ system for $-t < 0.4\ (GeV/c)^2$ and $\cos\lambda$ less than 0.5. Shaded events have $-t < 0.1\ (GeV/c)^2$.

Figs.10-12 t-distribution of the isospin 1/2 component of the $N\pi$ system with $\cos\lambda$ less than 0.5 for various $N\pi$ mass regions as follows: Fig.10: $m_{N\pi} < 1.3$ GeV, Fig.11: $1.3 < m_{N\pi} < 1.5$ GeV, Fig.12: $1.5 < m_{N\pi} < 1.8$ GeV

Fig.13 Scatter plots of $-t'_p$ vs $\pi^+\pi^0$ mass squared. The value of $-t'_p$ is the momentum transfer squared between incident and final proton minus the kinematic minimum corresponding to each particular value of $\pi^+\pi^0$ mass. These plots correspond to various ranges of $\cos\alpha$, where α is the $\pi\pi$ decay angle in the Jackson frame, as

follows: a) $1 \geq \cos\alpha \geq 0.8$, b) $0.8 \geq \cos\alpha \geq 0.6$, c) $0.6 \geq \cos\alpha \geq 0.4$, d) $0.4 \geq \cos\alpha \geq 0.2$, e) $0.2 \geq \cos\alpha \geq 0$.

Fig.14 Same as Fig.13 for the following angular regions: a) $-0.8 \geq \cos\alpha \geq -1$, b) $-0.6 \geq \cos\alpha \geq -0.8$, c) $-0.4 \geq \cos\alpha \geq -0.6$, d) $-0.2 \geq \cos\alpha \geq -0.4$, e) $-0.2 \leq \cos\alpha \leq 0$.

Fig.15 $\pi^+\pi^0$ mass spectrum with $-t_p \leq 0.5$ GeV/c^2 and $|\cos\alpha| \leq 0.5$. The curve is the fit discussed in the text. Although the bins shown are the ones used in the fit and are not all the same size, the ordinates do give events per unit bin width.

Fig.16 $d\sigma/dt'$ distribution for the final state ρ^+p.

Fig.17 $\pi^+\pi^0$ mass spectrum for $2 \leq -t'_p \leq 4$ (GeV/c)^2. The solid curve is the fit including ρ^+ production plus background. The dashed curve is the background contribution to the fit. Variable bin size is used here as in Fig.15.

Fig.18 Same as Fig.17 for a different t'_p region; namely $-t'_p \geq 4$ (GeV/c)^2. Variable bin size is used here as in Fig.15

Fig.19 Density matrix elements as a function of t'_p for the reaction $\pi^+p \to \rho^+p$ in the Gottfried-Jackson frame. The solid crosses come from the fits discussed in the text. The dashed crosses are calculated by taking a $\pi^+\pi^0$ mass selection of 0.66 - 0.86 GeV only.

Fig.20 Density matrix elements as a function of t'_p for the ρ^+ from the reaction $\pi^+p \to \rho^+p$ in the s-channel or helicity frame. The solid crosses come from the fits discussed in the text. The dashed crosses are calculated by taking a $\pi^+\pi^0$ mass selection of .66 - .86 GeV only.

Fig.21 Dalitz plot for the final state $p\pi^+\pi^o$ with $-t'_p < 0.08$ $(GeV/c)^2$.

Fig.22 $\pi^+\pi^o$ mass spectrum with $0.08 < -t'_p < 0.5$ $(GeV/c)^2$ and $\cos\alpha < 0$ and ϕ (Treiman-Yang angle) in one of the following intervals: $45^o < \phi < 135^o$, $225^o < \phi < 315^o$. The solid curve is the fit including ρ^+ production plus background. The dashed curve is the background contribution to the fit. Variable bin size is used here as in Fig.15.

Fig.23 $\pi^+\pi^o$ mass spectrum with $0.08 < -t'_p < 0.5 (GeV/c)^2$ and $\cos\alpha < 0$ and ϕ (Treiman-Yang angle) in one of the following intervals: $0^o < \phi < 45^o$, $135^o < \phi < 225^o$, $315^o < \phi < 360^o$. The solid curve is the fit including ρ^+ production plus background. The dashed curve is the background contribution to the fit. Variable bin size is used here as in Fig.15.

Fig.24 a) $\rho_{oo} d\sigma/dt'$ b) $(\rho_{11} + \rho_{1-1})\, d\sigma/dt'$ c) $(\rho_{11} - \rho_{1-1})\, d\sigma/dt'$ (Jackson frame) for ρ^+ production as a function of t'_p.

Fig.25 a) $n\pi^+$ mass spectrum b) $p\pi^o$ mass spectrum. Shaded events have $|t_{\pi+}|$ <u>greater</u> than 0.5 $(GeV/c)^2$.

Fig.26 Scatter plot of $-t_p$ vs $\pi^+\pi^o$ mass squared with events with $1.16 < m_{p\pi^+} < 1.3$ $(GeV/c)^2$ and $-t_{\pi^o} < 0.4$ $(GeV/c)^2$ and also events with $m_{p\pi^o} < 1.7$ GeV and $-t_{\pi^+} < 0.4$ $(GeV/c)^2$ removed.

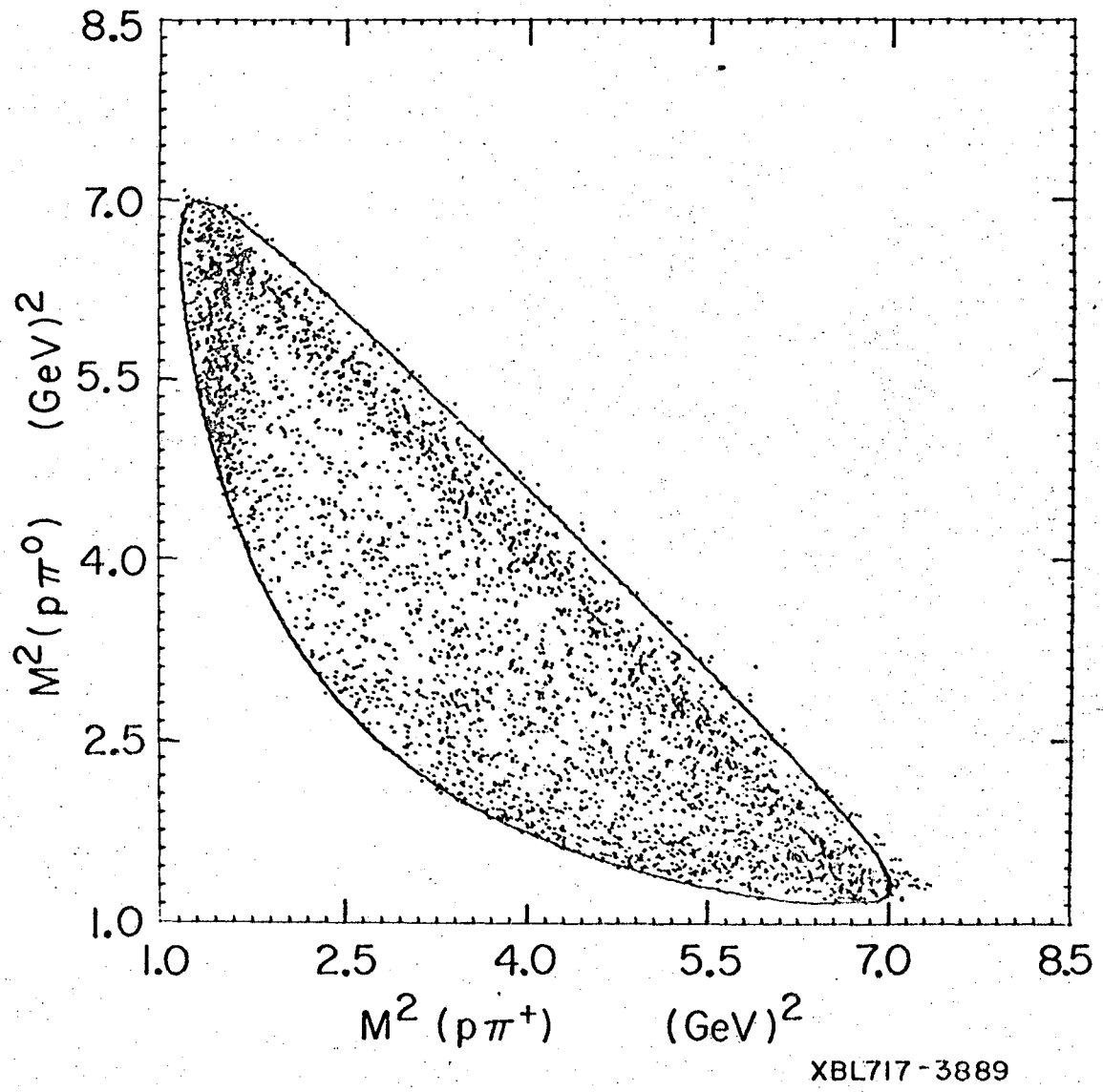
8.5
7.0
5.5
4.0
2.5
1.0
$M^2(p\pi^0)$ $(GeV)^2$
1.0
2.5
4.0
5.5
7.0
8.5
$M^2(p\pi^+)$ $(GeV)^2$
XBL717-3889

Fig. 1

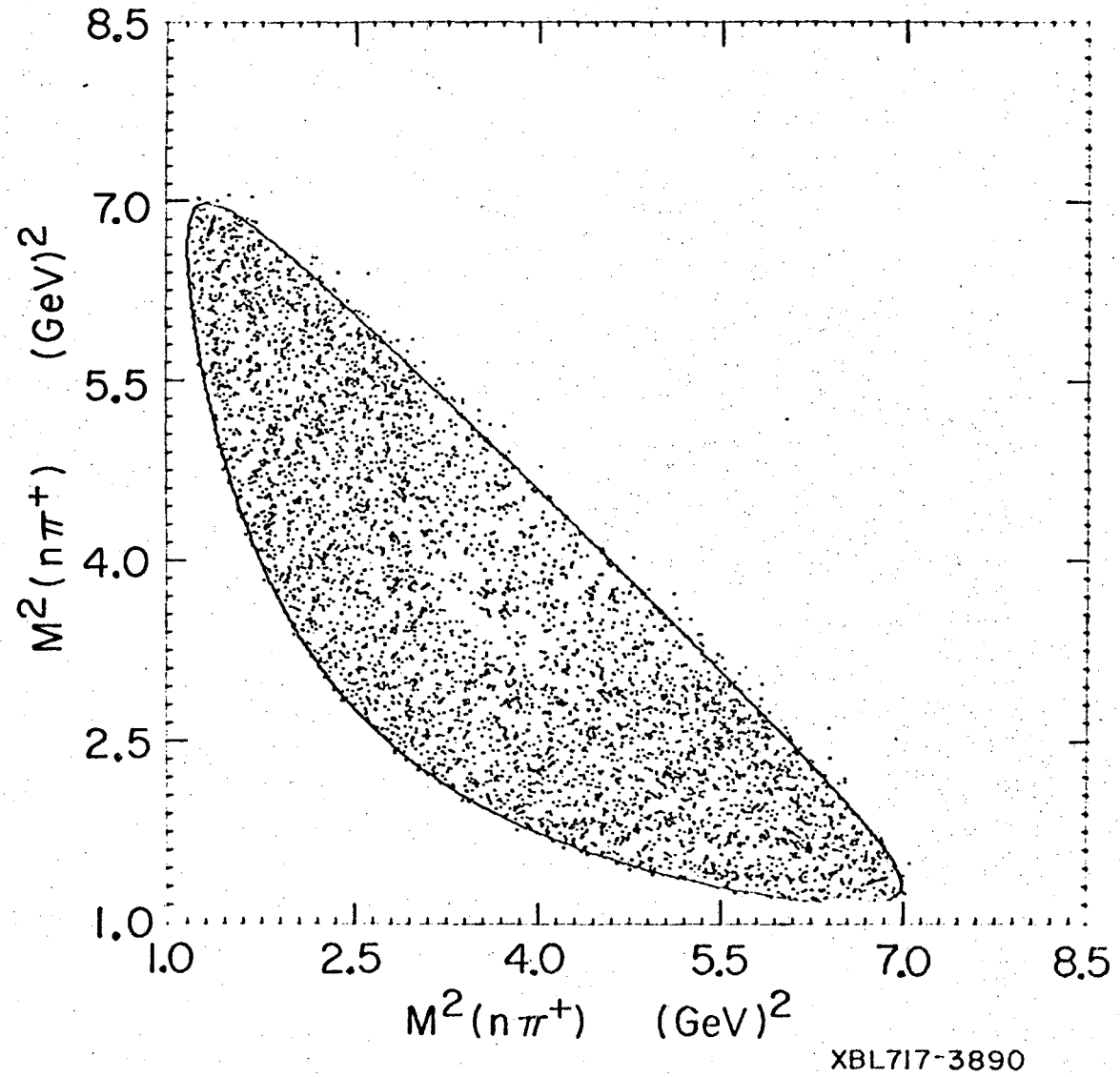
8.5
7.0
5.5
4.0
2.5
1.0
$M^2(n\pi^+)$ $(GeV)^2$
1.0
2.5
4.0
5.5
7.0
8.5
$M^2(n\pi^+)$ $(GeV)^2$
XBL717-3890

Fig. 2

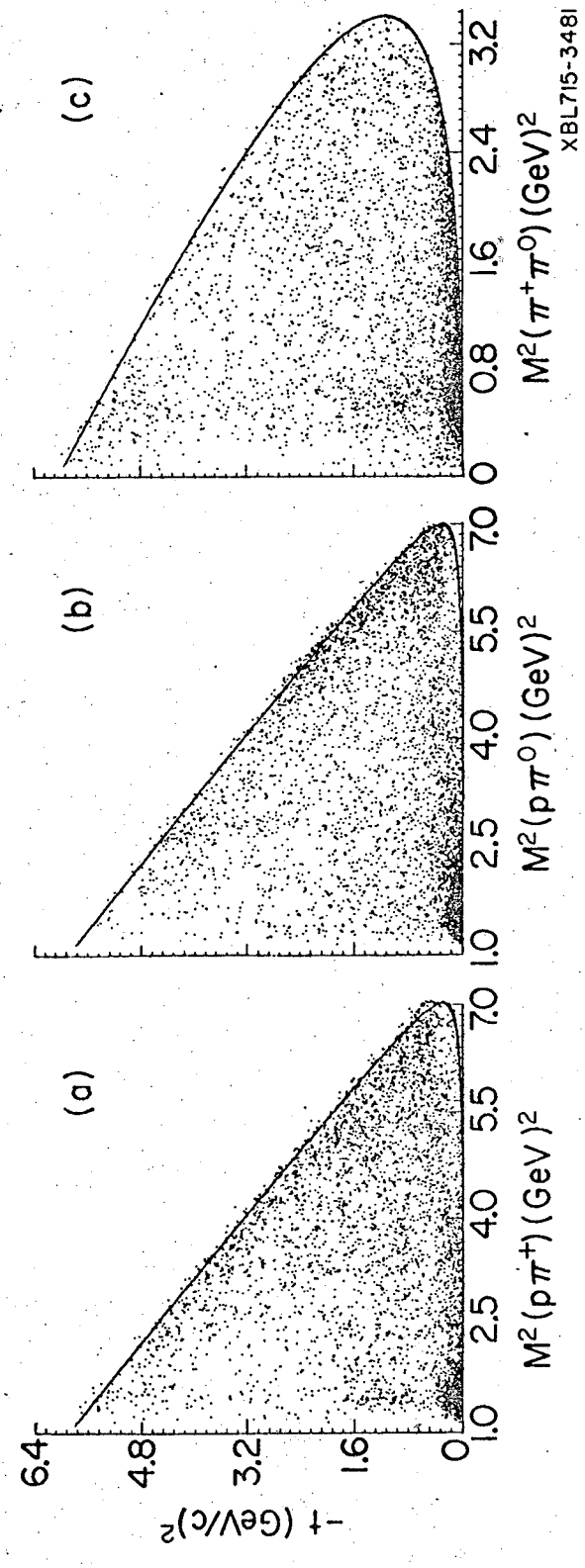
(a)
(b)
(c)
-t (GeV/c)²
6.4
4.8
3.2
1.6
0
1.0
2.5
4.0
5.5
7.0
0
0.8
1.6
2.4
3.2
M²(pπ⁺) (GeV)²
M²(pπ⁰) (GeV)²
M²(π⁺π⁰) (GeV)²
XBL715-3481

Fig. 3

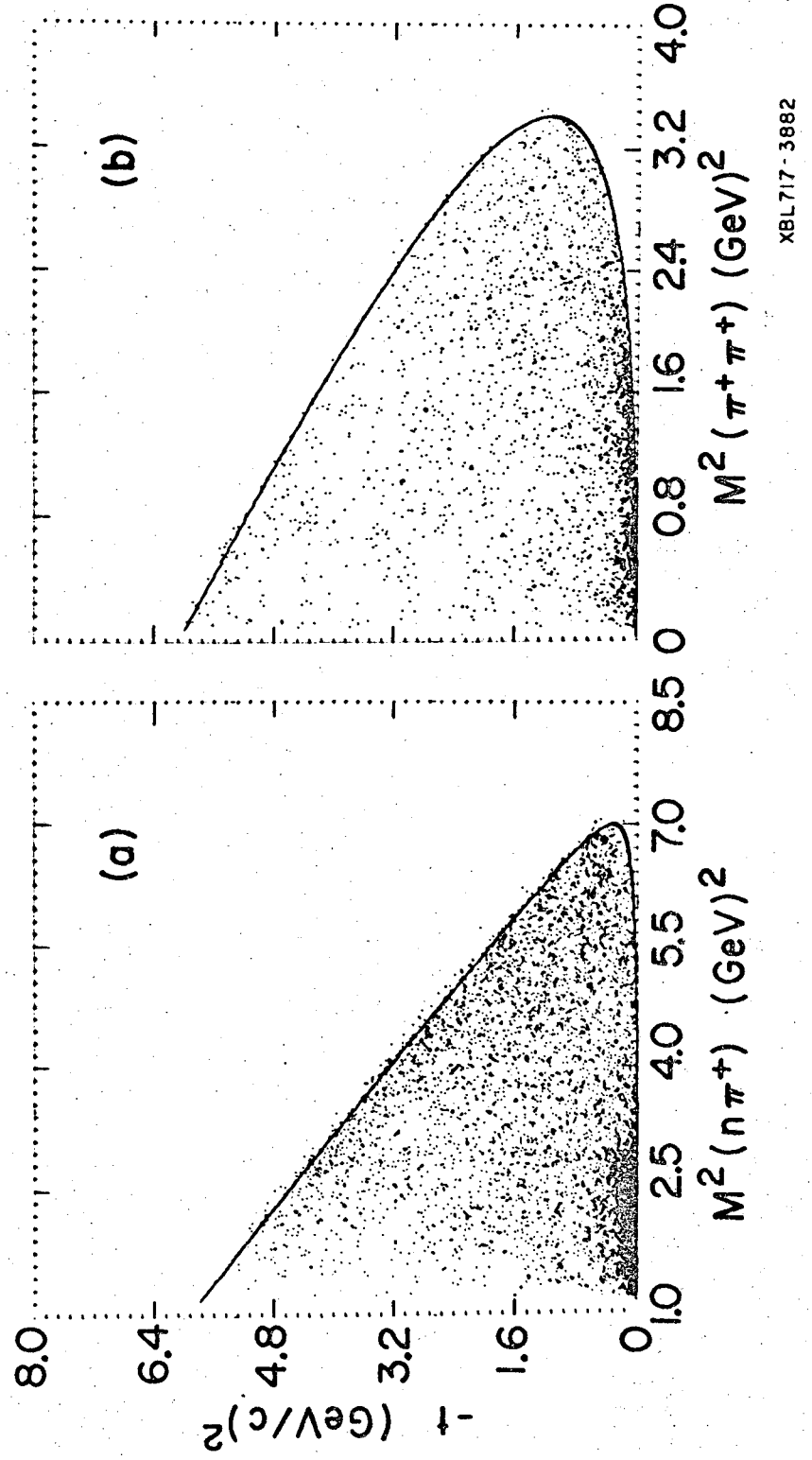

Fig. 4

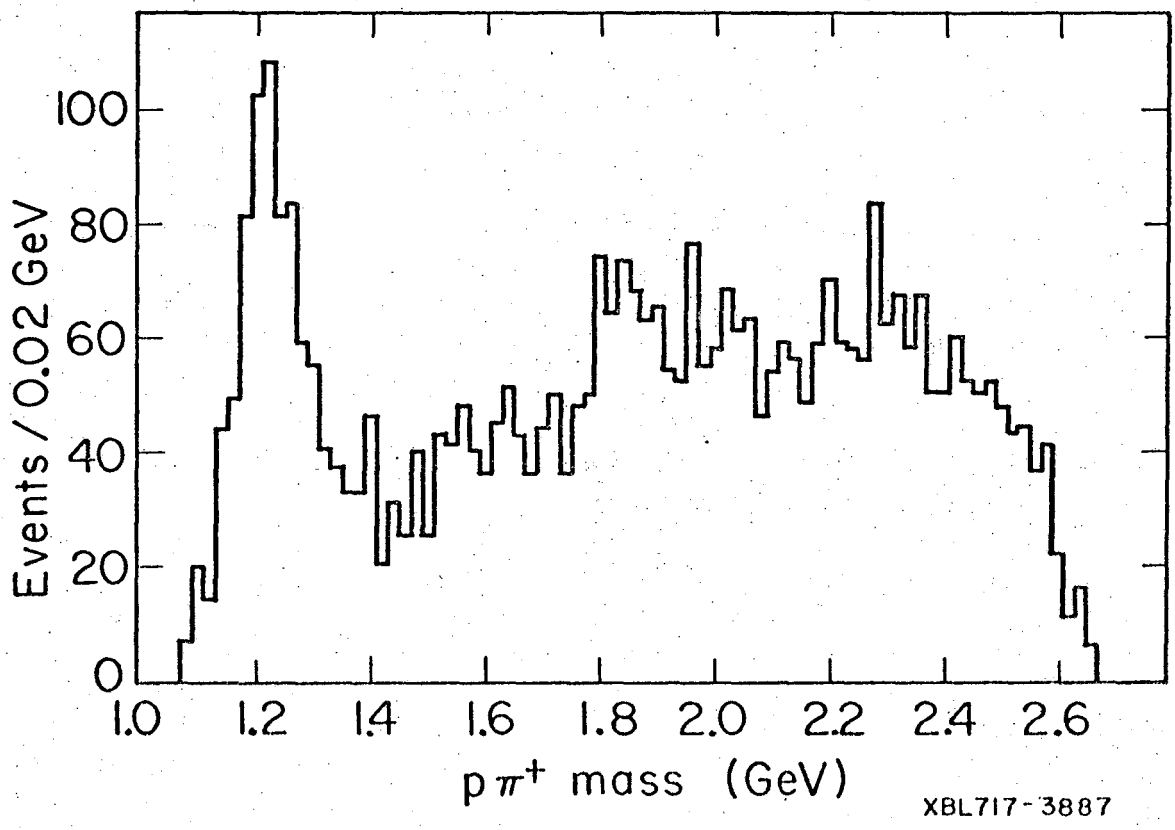
Events / 0.02 GeV
0
20
40
60
80
100
1.0
1.2
1.4
1.6
1.8
2.0
2.2
2.4
2.6
p π+ mass (GeV)
XBL717-3887

Fig. 5

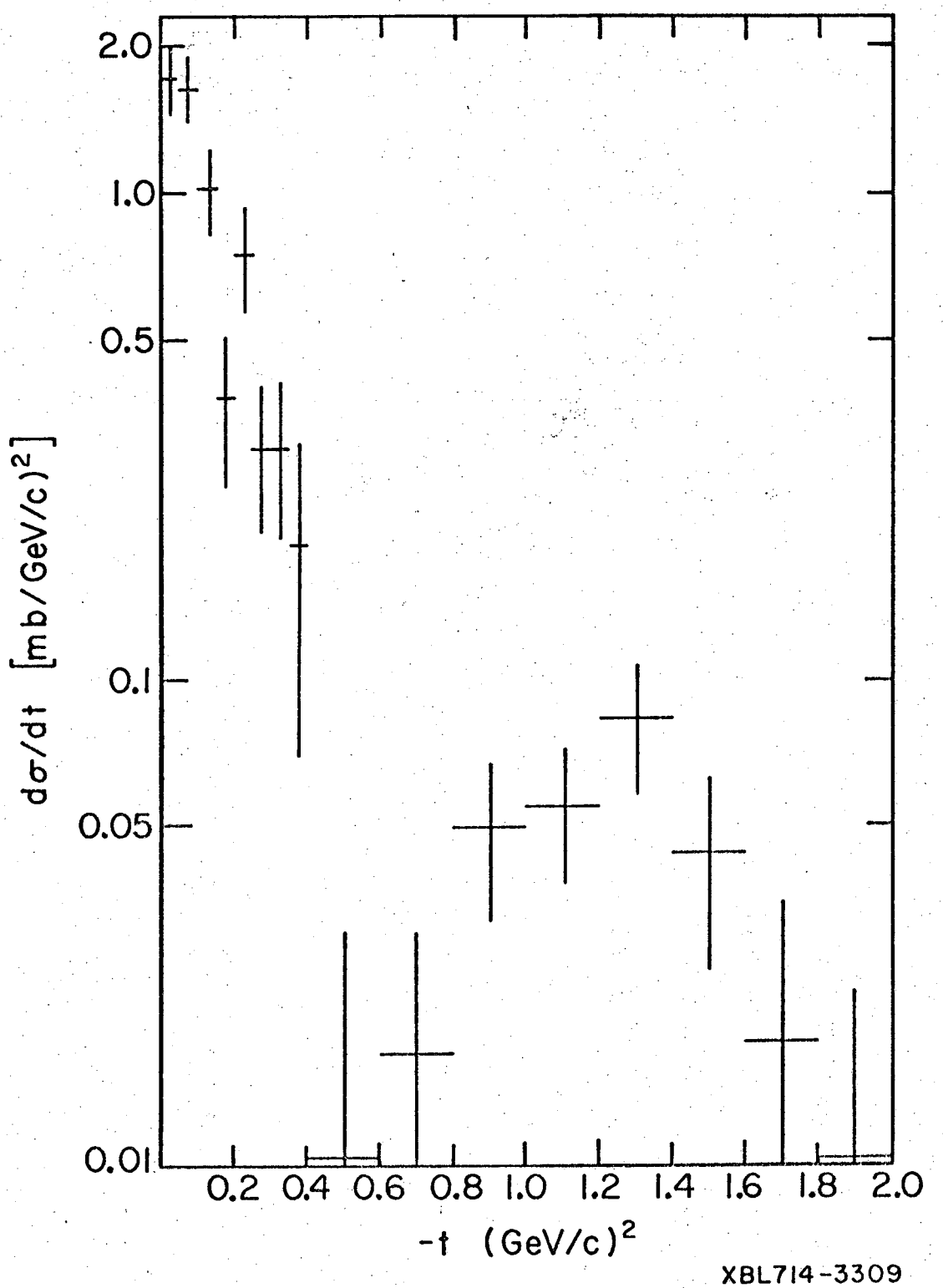
2.0
1.0
0.5
0.1
0.05
0.01
dσ/dt [mb/GeV/c)²]
0.2 0.4 0.6 0.8 1.0 1.2 1.4 1.6 1.8 2.0
-t (GeV/c)²
XBL714-3309

Fig. 6

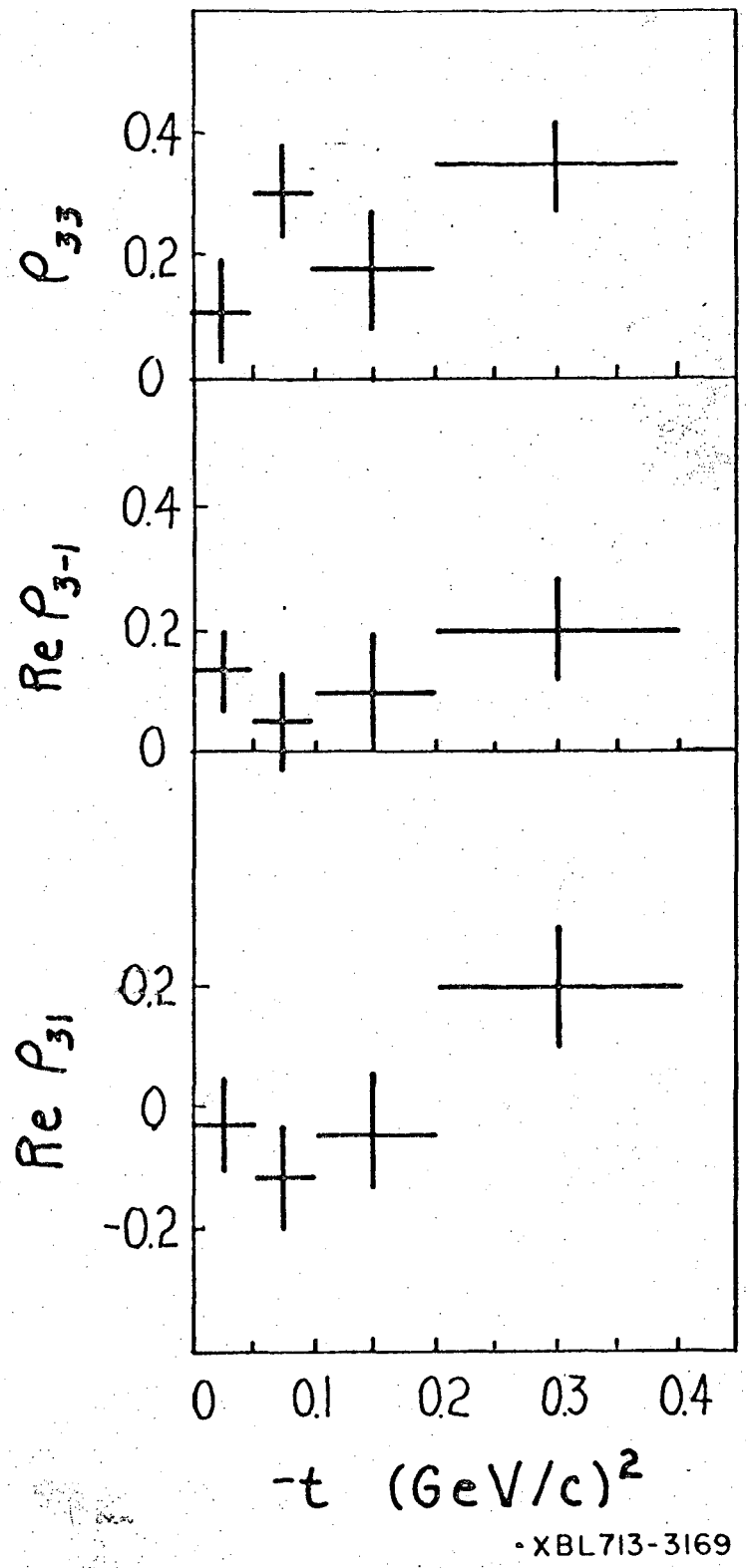
ρ_{33}
0.4
0.2
0
Re ρ_{3-1}
0.4
0.2
0
Re ρ_{31}
0.2
0
-0.2
0
0.1
0.2
0.3
0.4
$-t$ (GeV/c)^2
XBL713-3169

Fig. 7

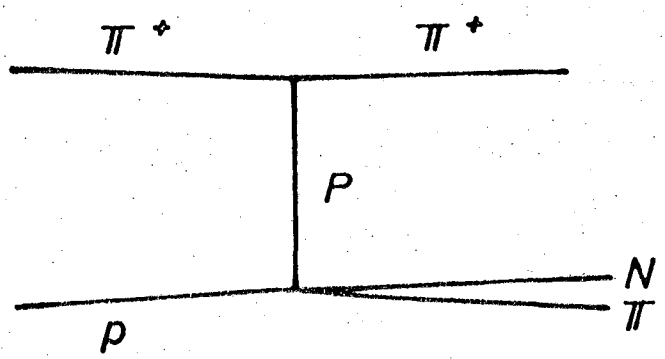

Fig. 8

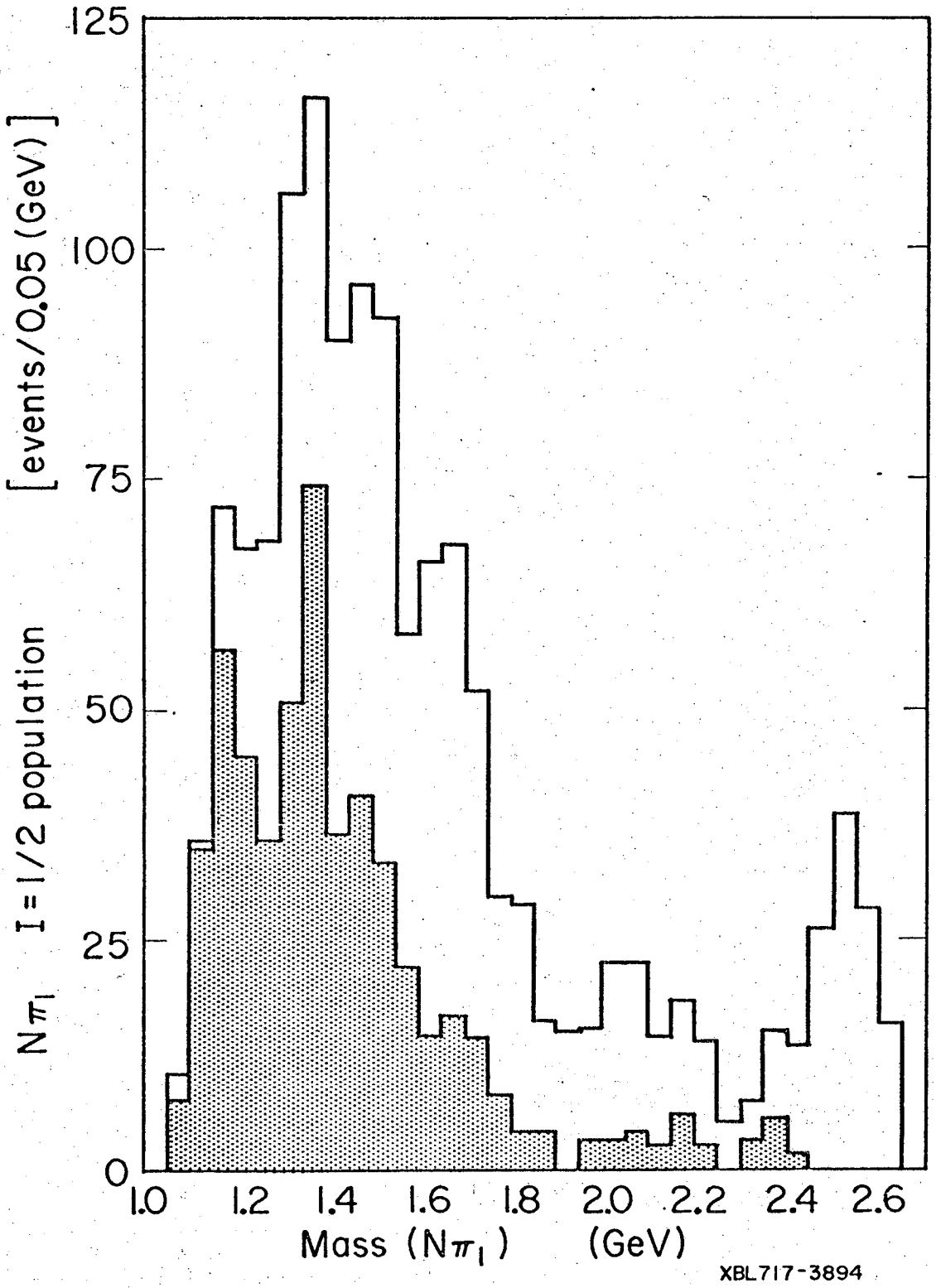
125
100
75
50
25
0
[events/0.05 (GeV)]
Nπ1 I=1/2 population
1.0
1.2
1.4
1.6
1.8
2.0
2.2
2.4
2.6
Mass (Nπ1) (GeV)
XBL717-3894

Fig. 9

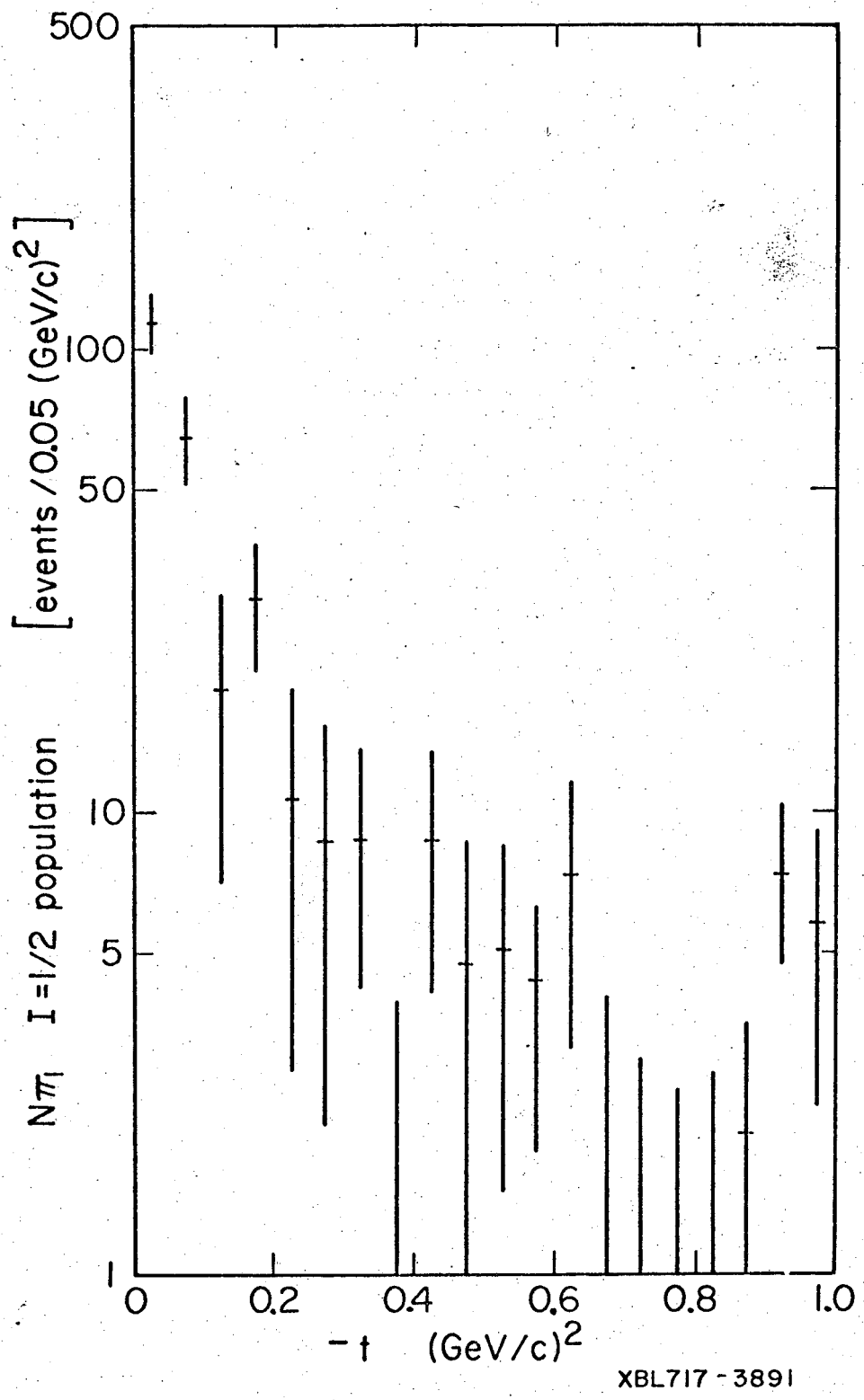
500
100
50
10
5
1
0
0.2
0.4
0.6
0.8
1.0
[events /0.05 (GeV/c)^2]
N_{π_1} I=1/2 population
$-t$ (GeV/c)^2
XBL717-3891

Fig. 1o

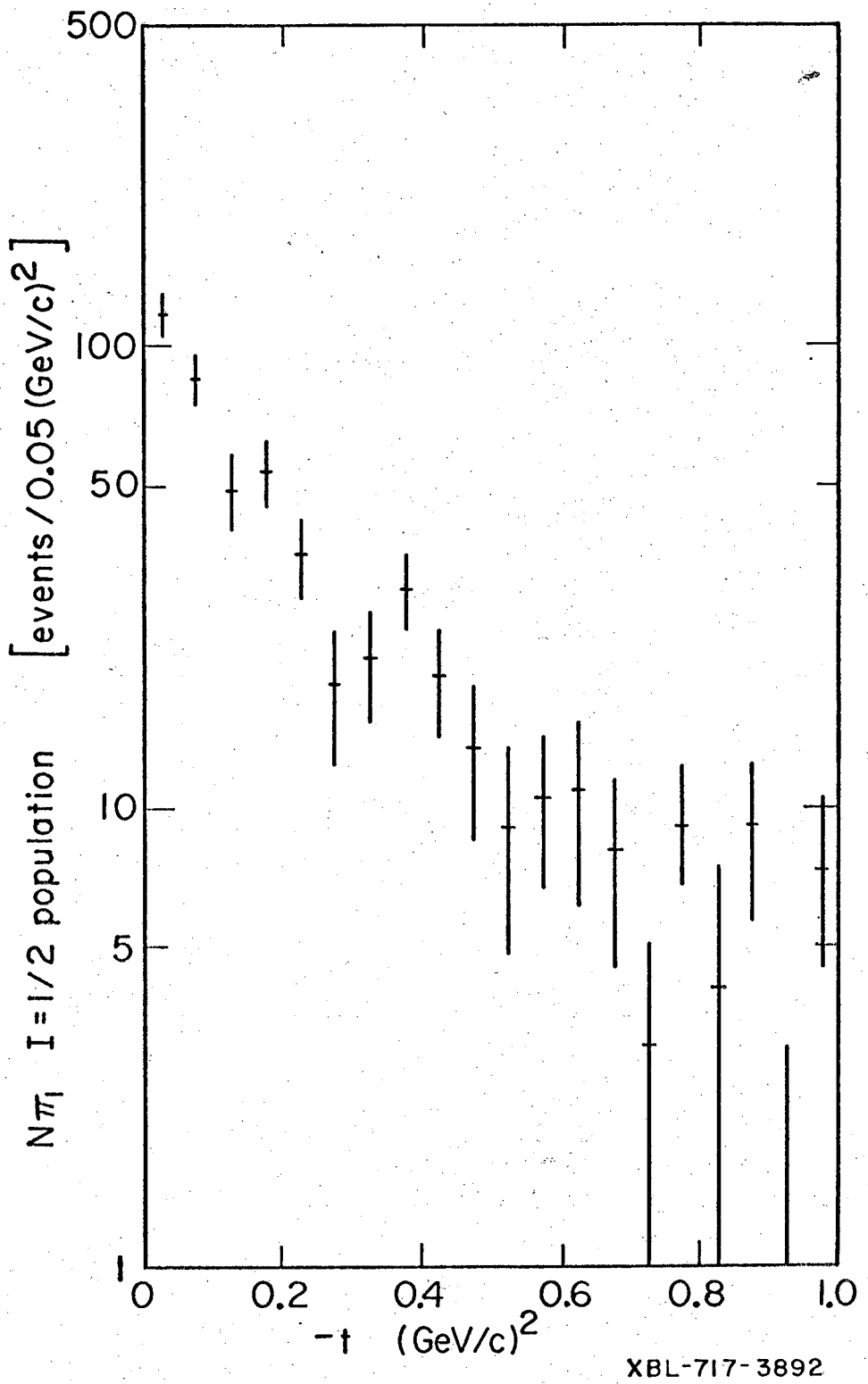
500
100
50
10
5
1
0
0.2
0.4
0.6
0.8
1.0
$N\pi_1$ I=1/2 population [events/0.05 (GeV/c)^2]
$-t$ (GeV/c)^2
XBL-717-3892

Fig. 11

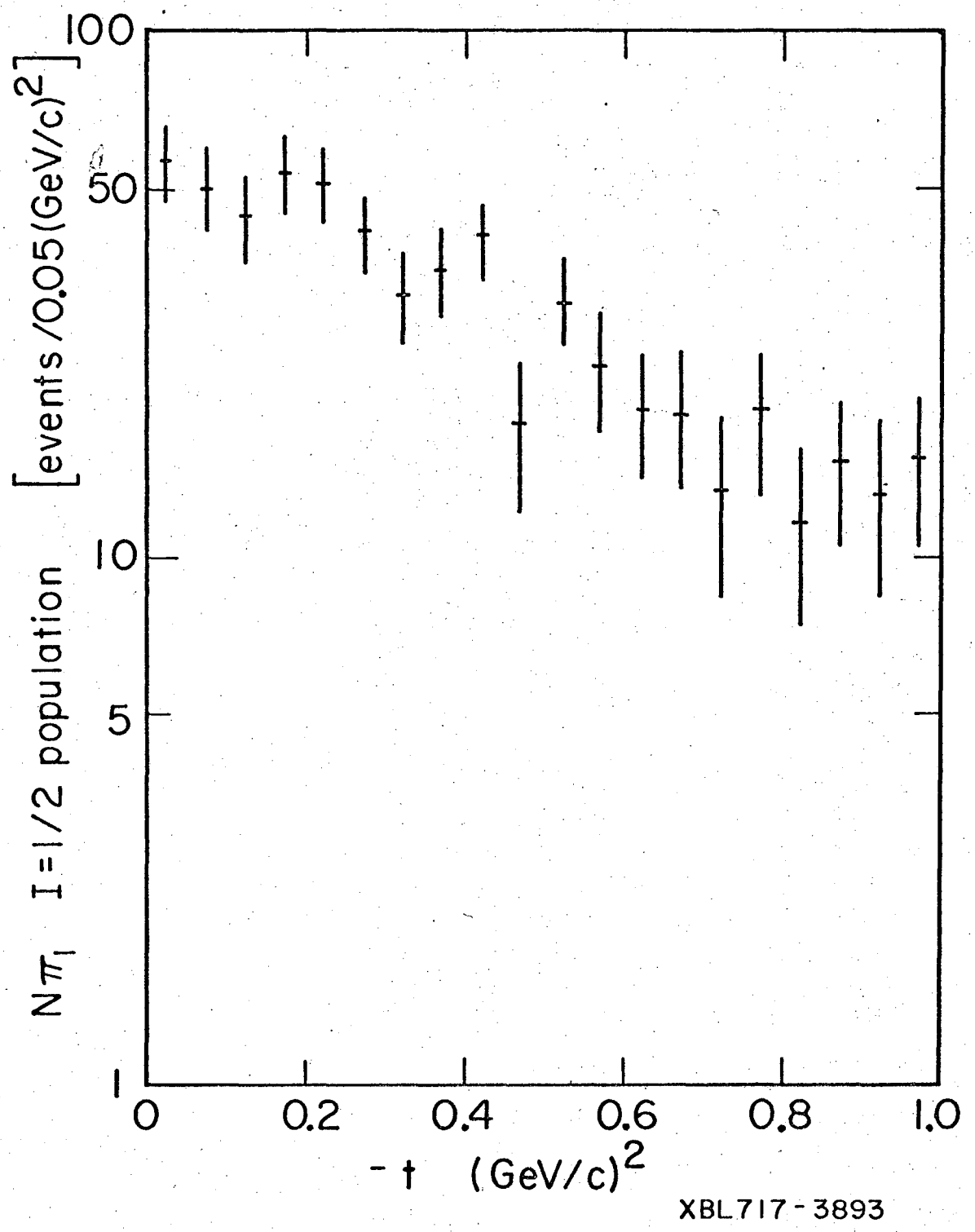
100
50
10
5
1
[events /0.05(GeV/c)^2]
$N\pi_1$ I=1/2 population
0
0.2
0.4
0.6
0.8
1.0
$-t$ (GeV/c)^2
XBL717-3893

Fig. 12

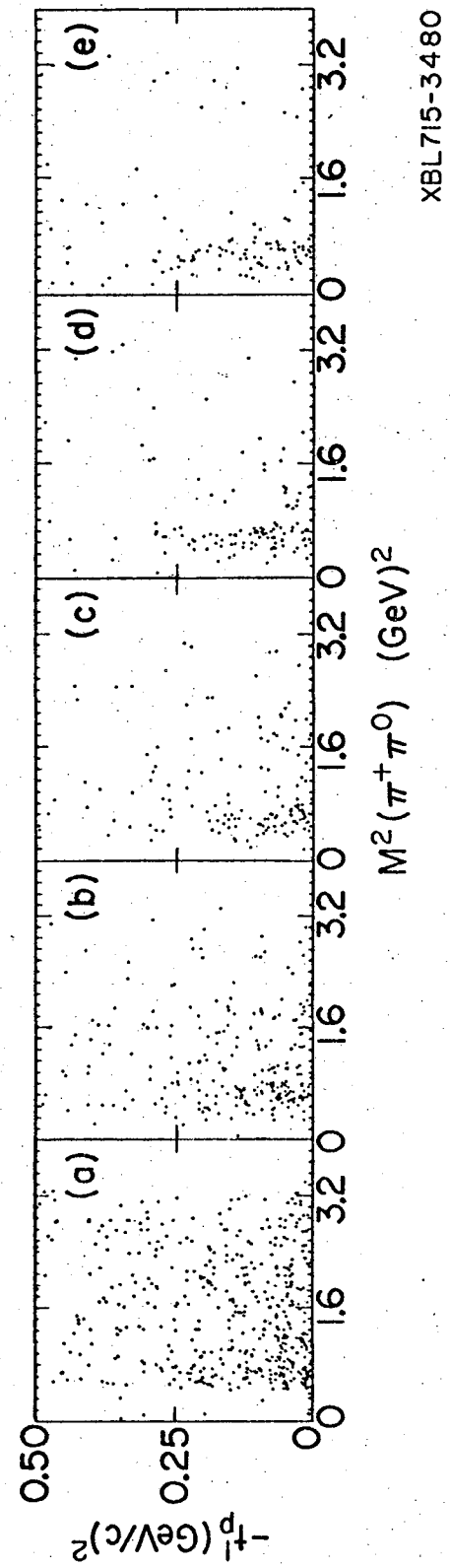

XBL715-3480

Fig. 13

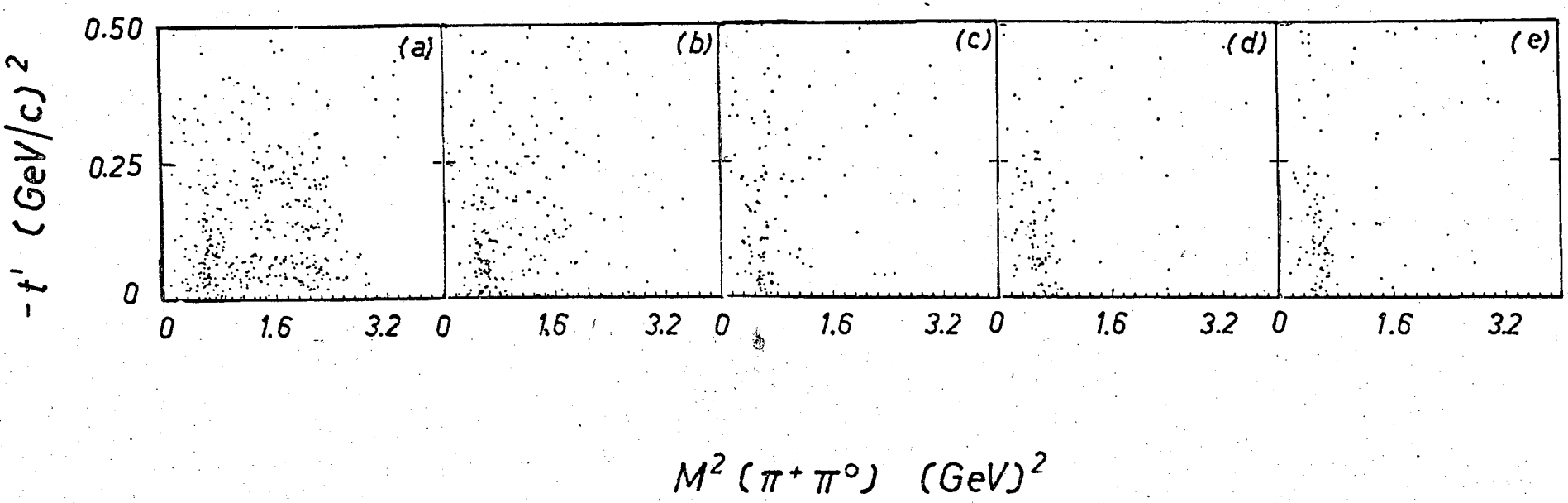

Fig. 14

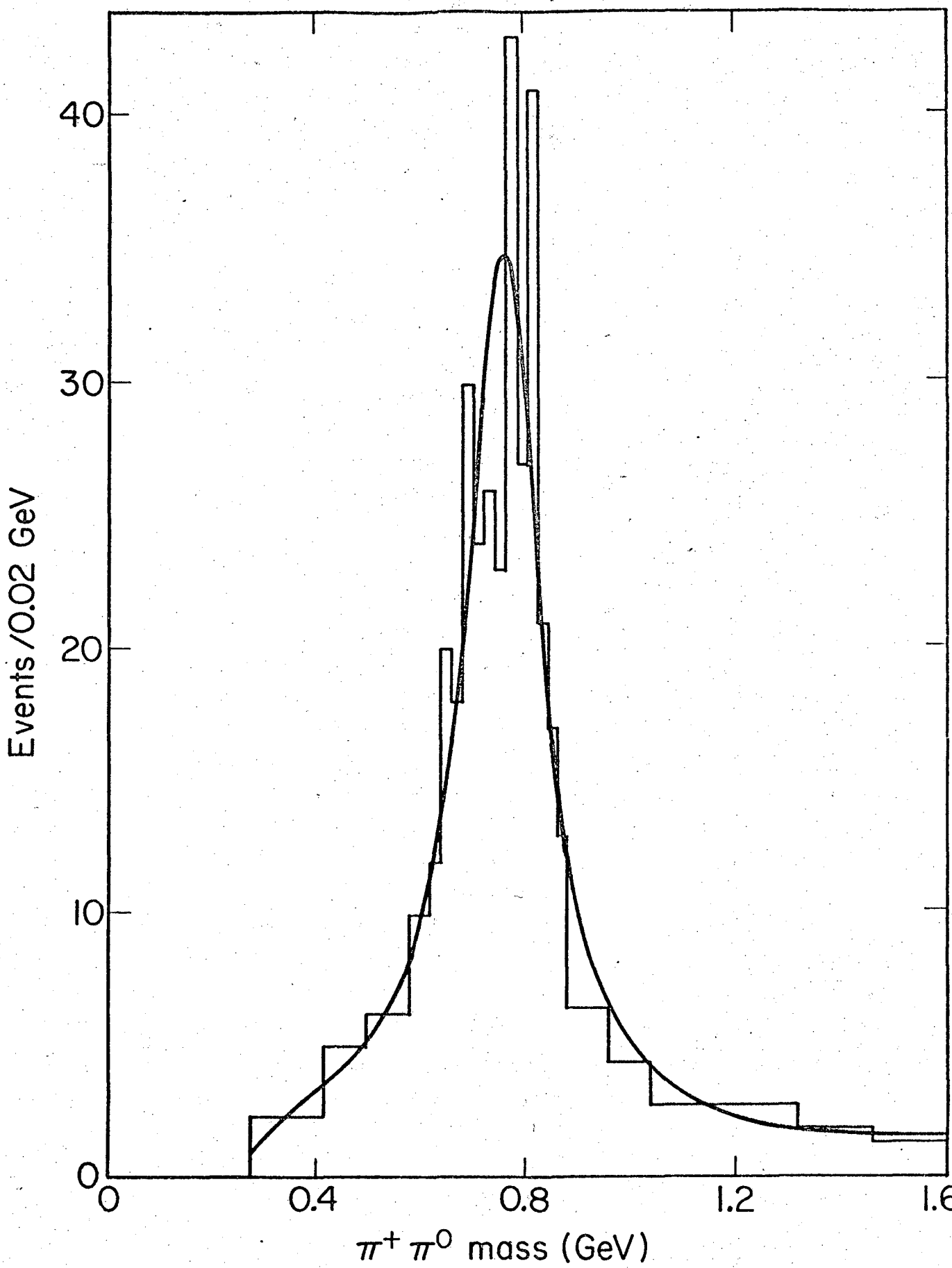

Fig. 15

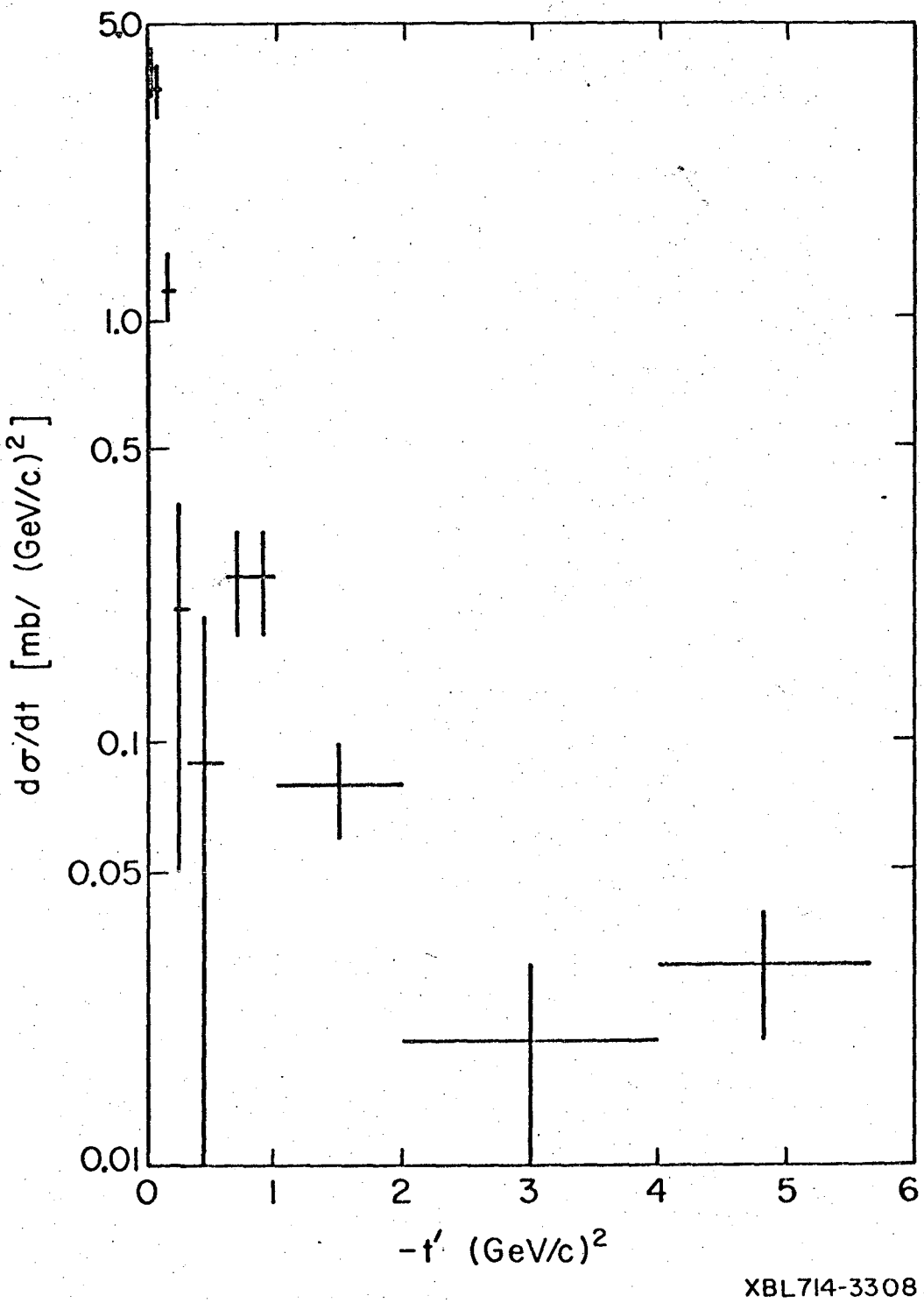

Fig. 16

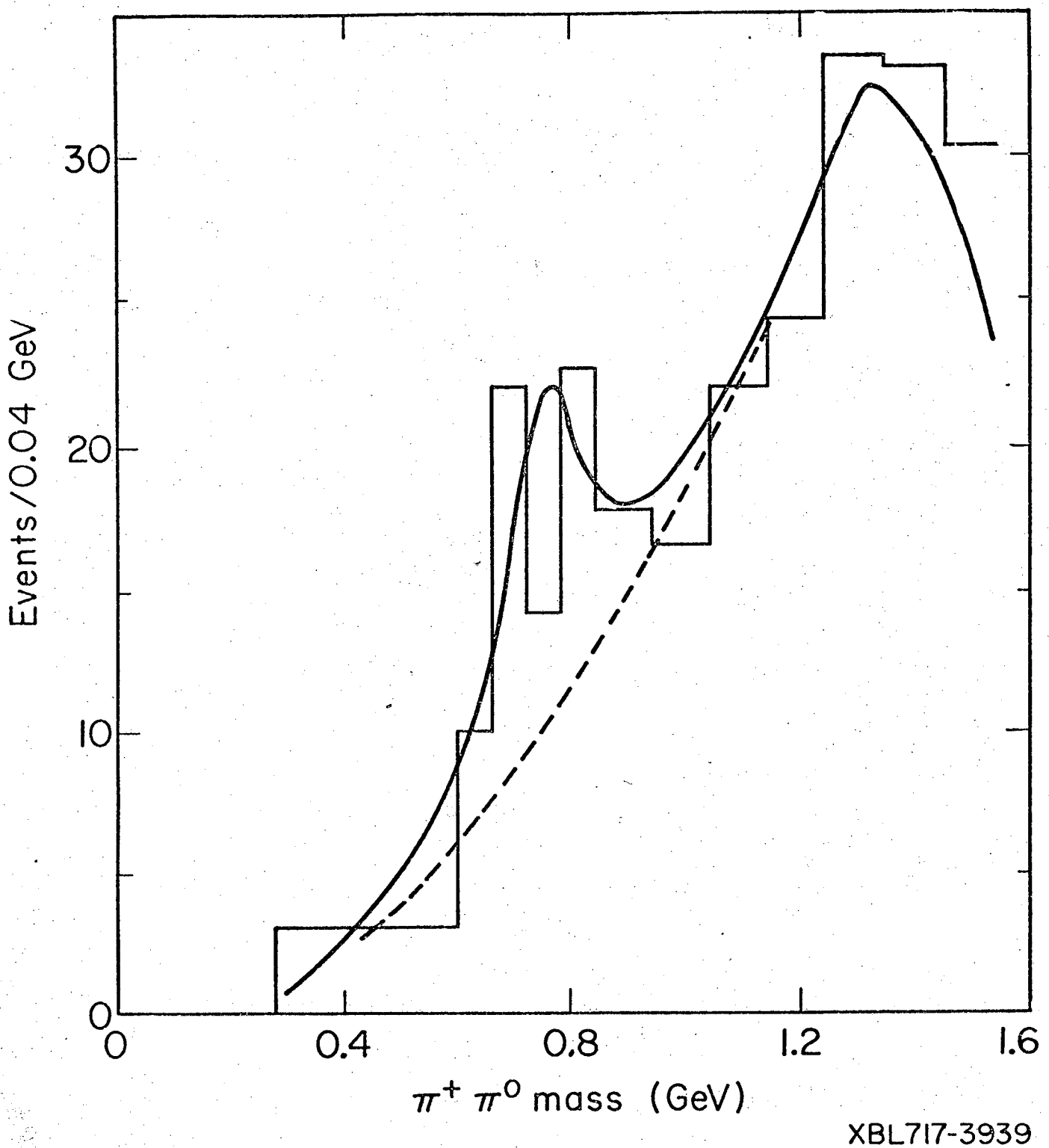
30
20
10
0
Events/0.04 GeV
0
0.4
0.8
1.2
1.6
$\pi^+ \pi^0$ mass (GeV)
XBL717-3939

Fig. 17

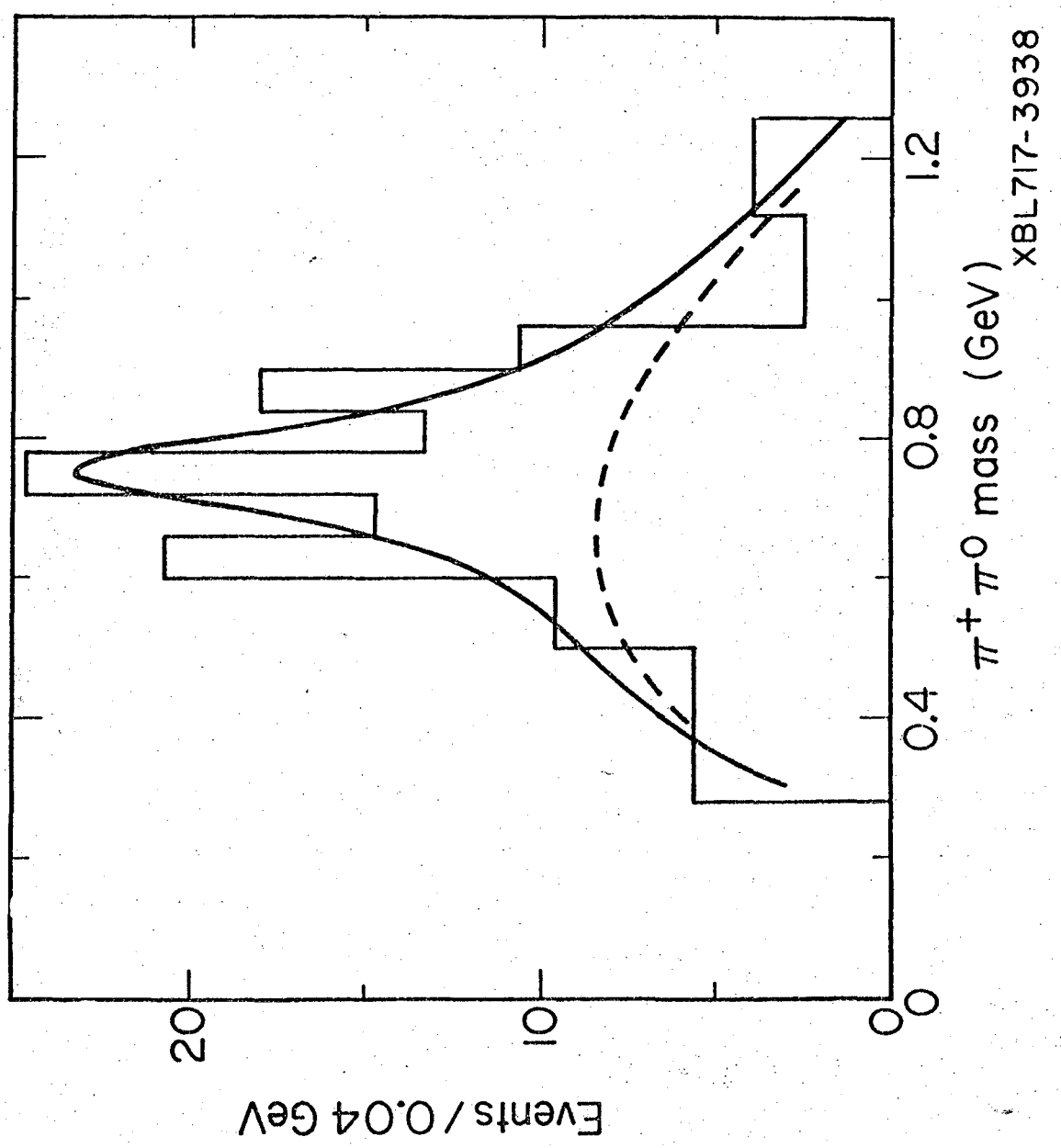

Fig. 18

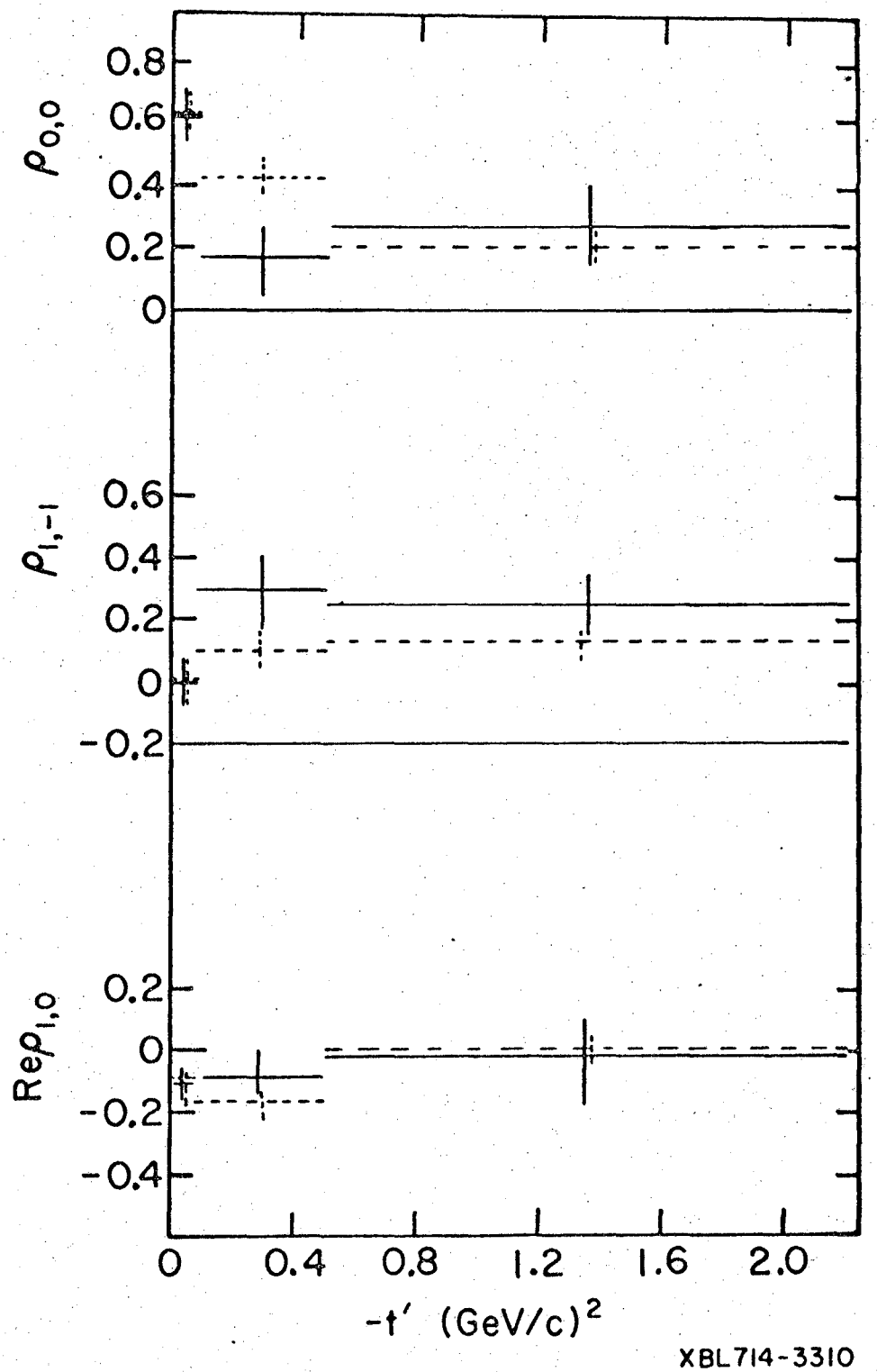

Fig. 19

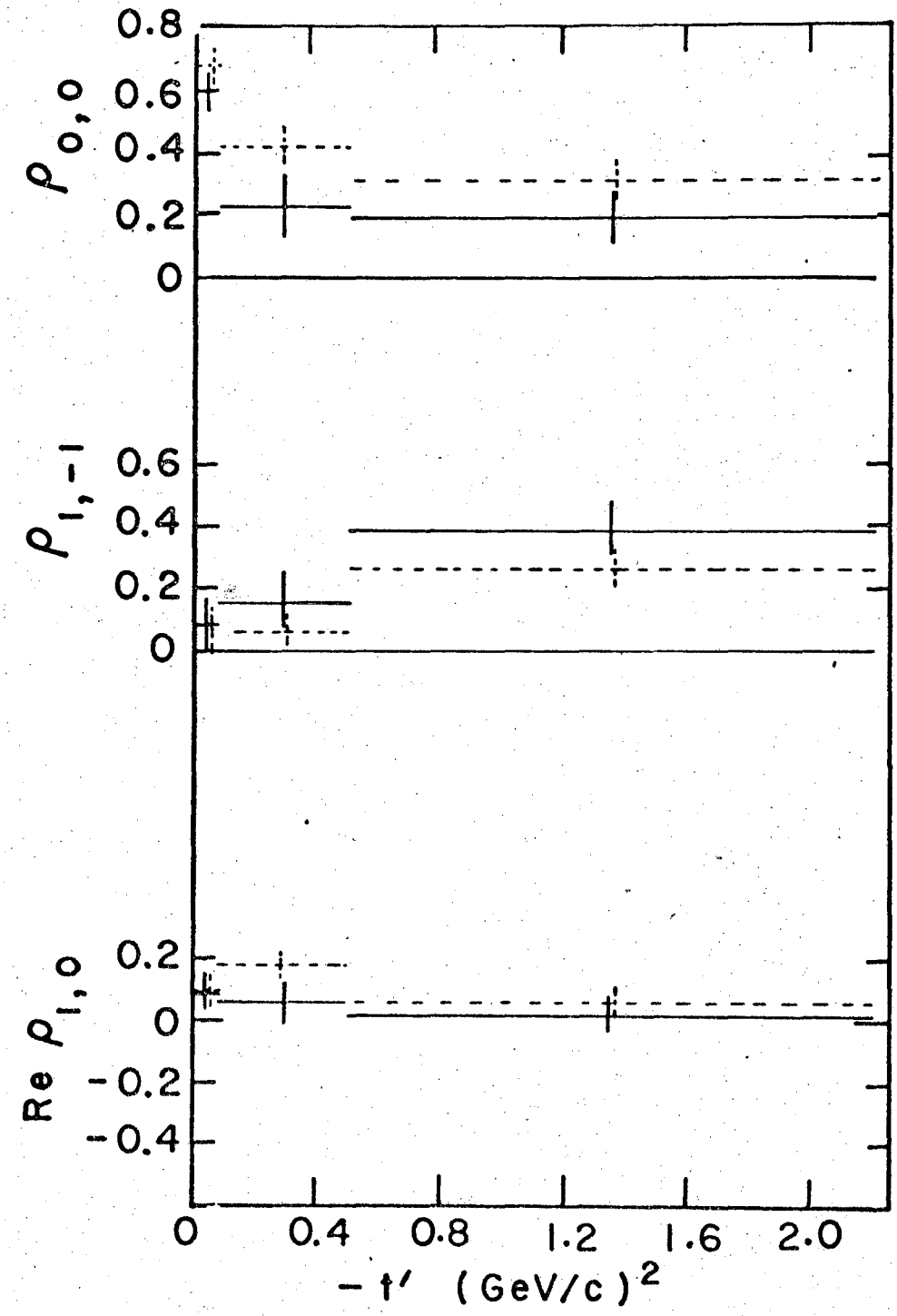

XBL714-3305

Fig. 2o

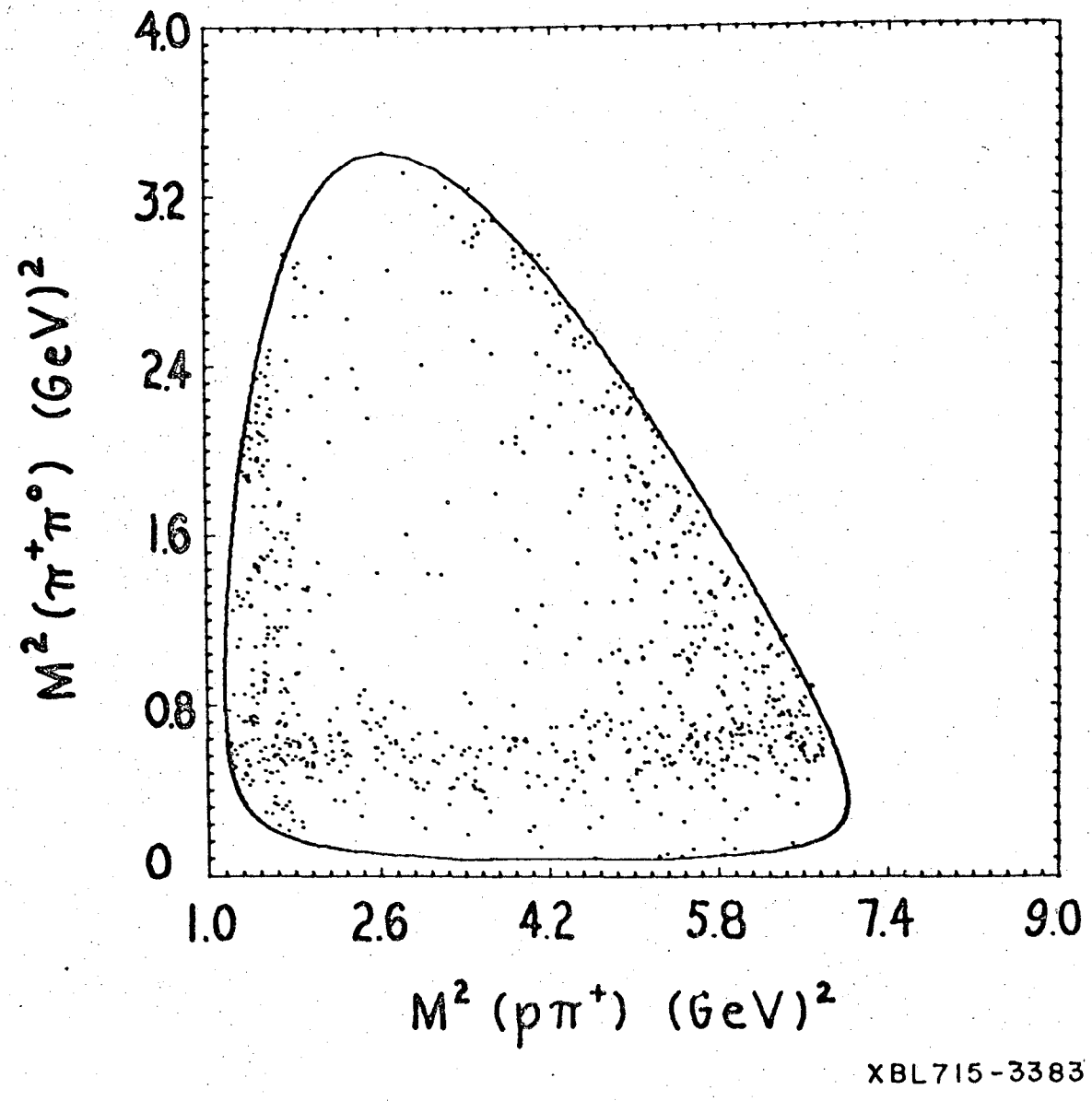

Fig. 21

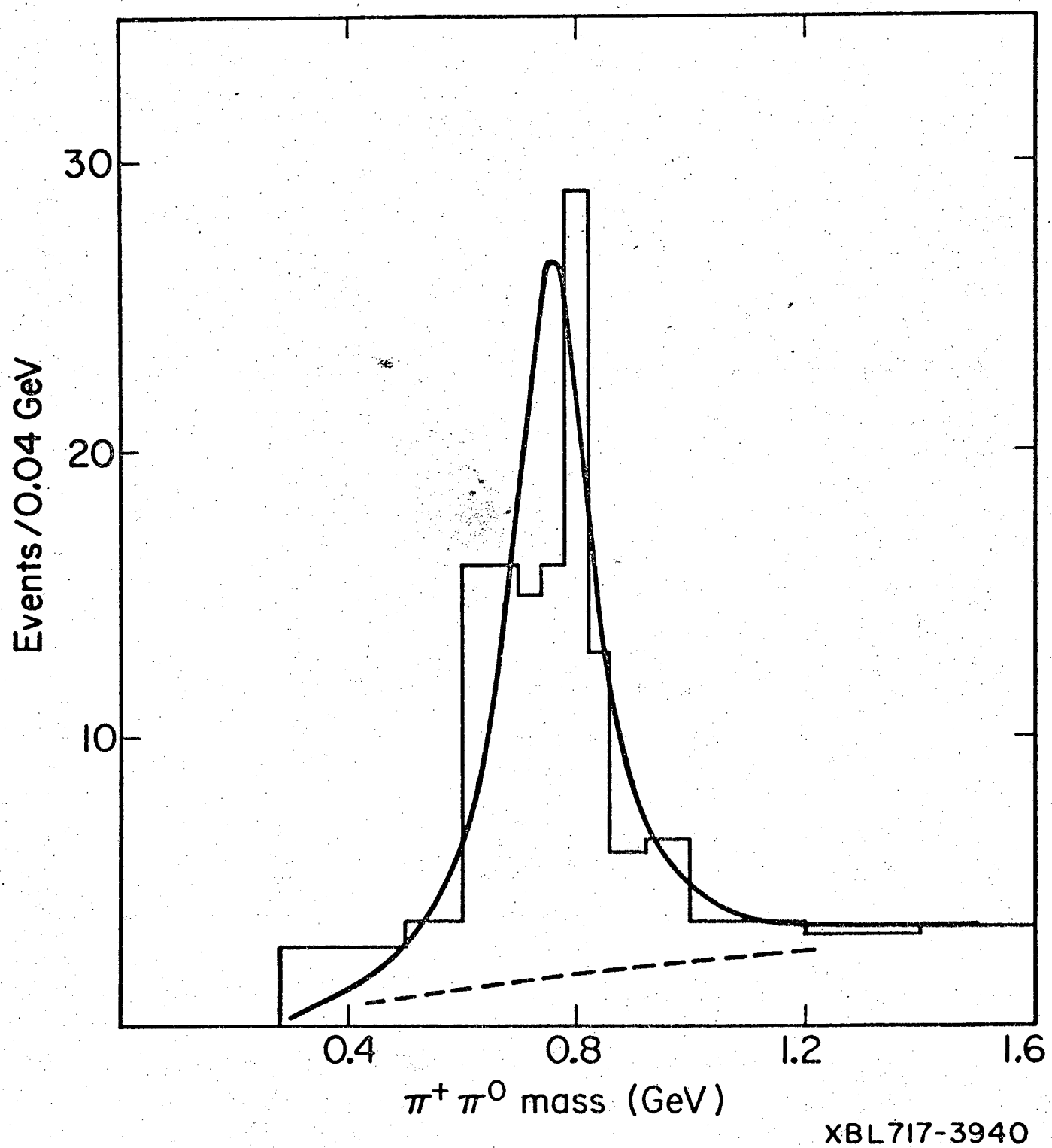

Fig. 22

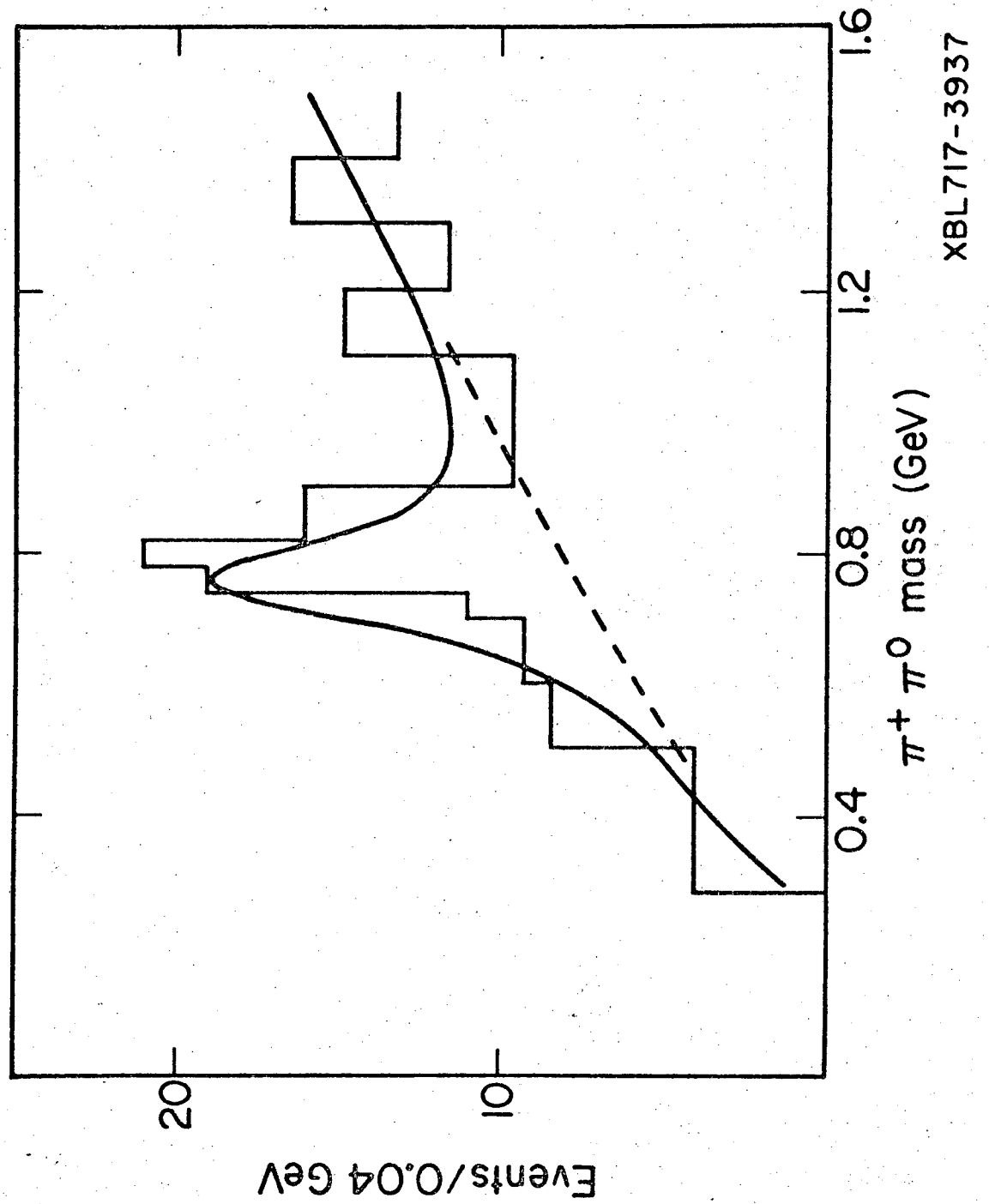

Fig. 23

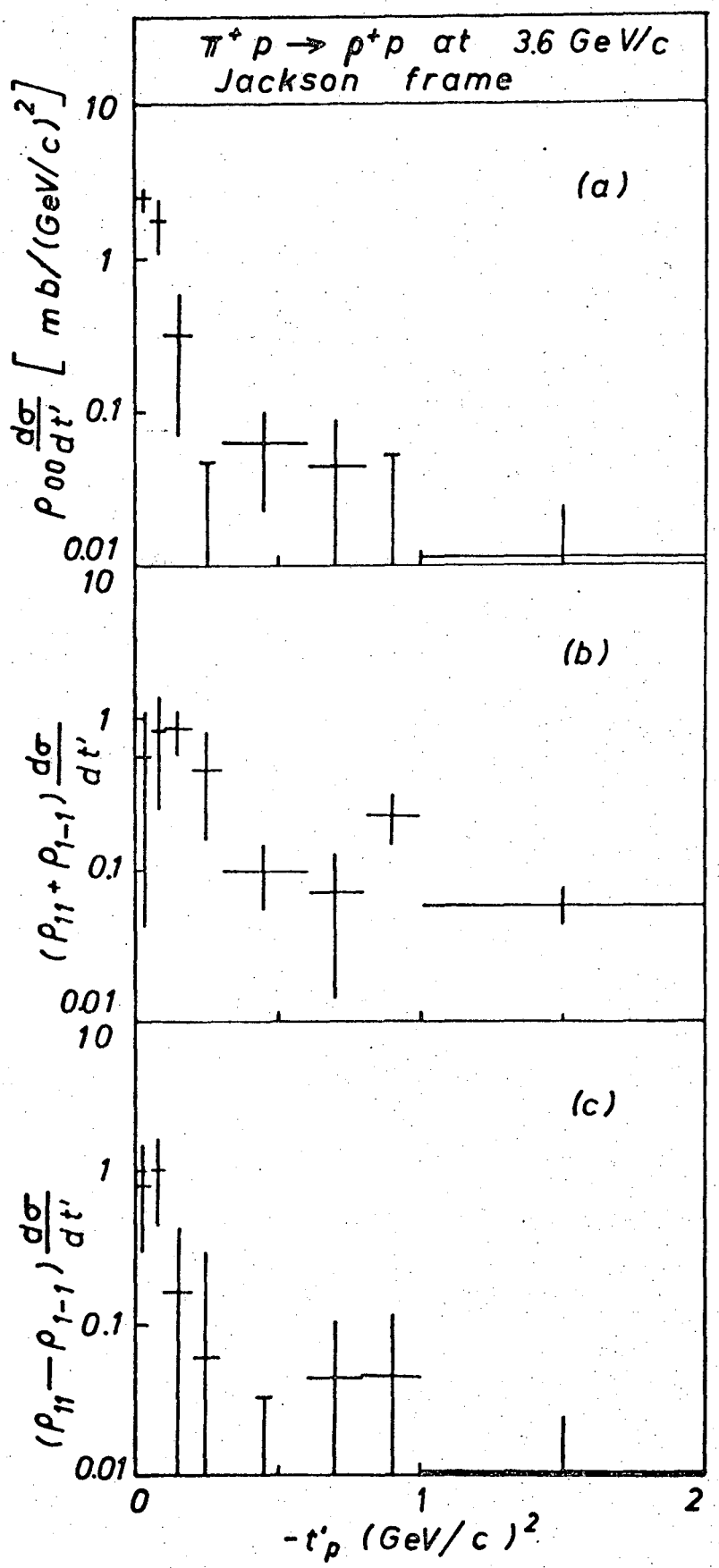

Fig. 24

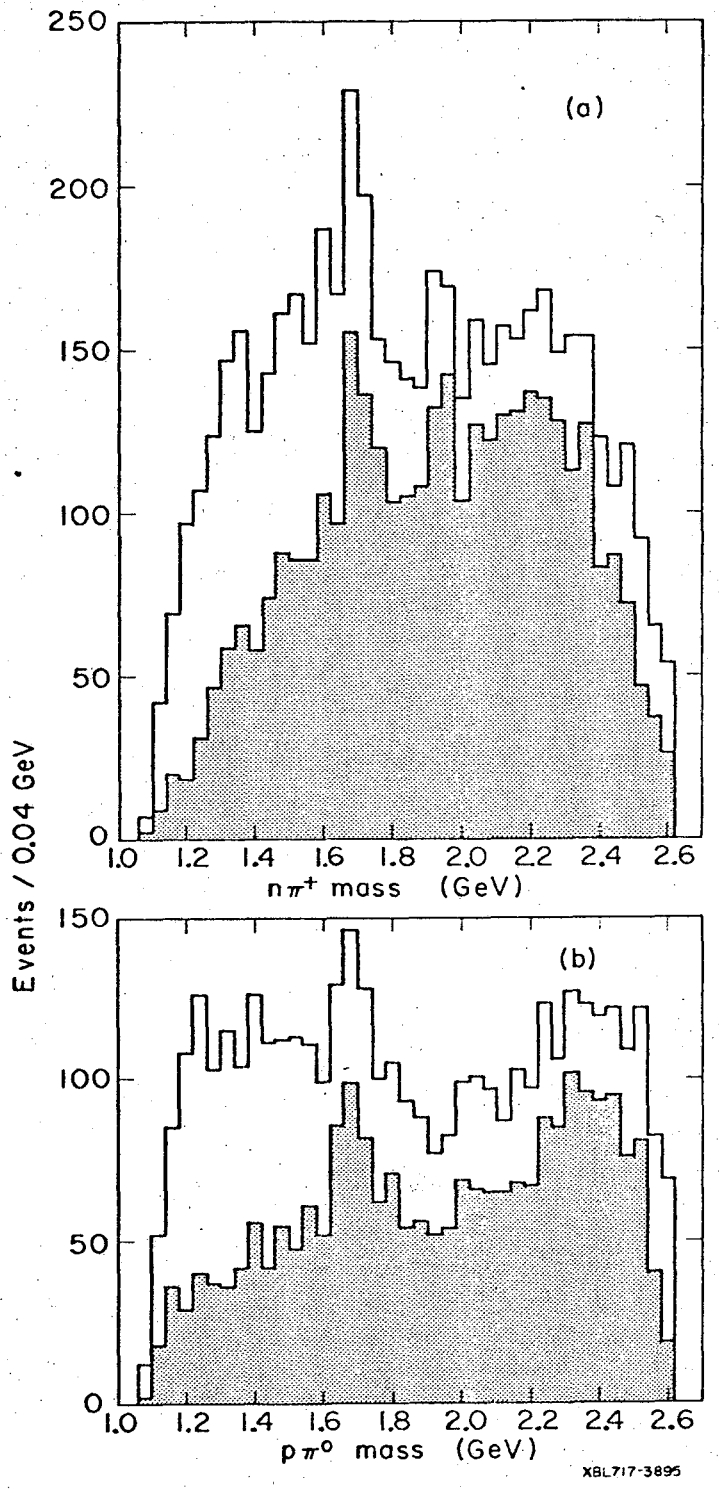
250
200
150
100
50
0
(a)
1.0 1.2 1.4 1.6 1.8 2.0 2.2 2.4 2.6
nπ+ mass (GeV)
Events / 0.04 GeV
150
100
50
0
(b)
1.0 1.2 1.4 1.6 1.8 2.0 2.2 2.4 2.6
pπ0 mass (GeV)
XBL717-3895

Fig. 25

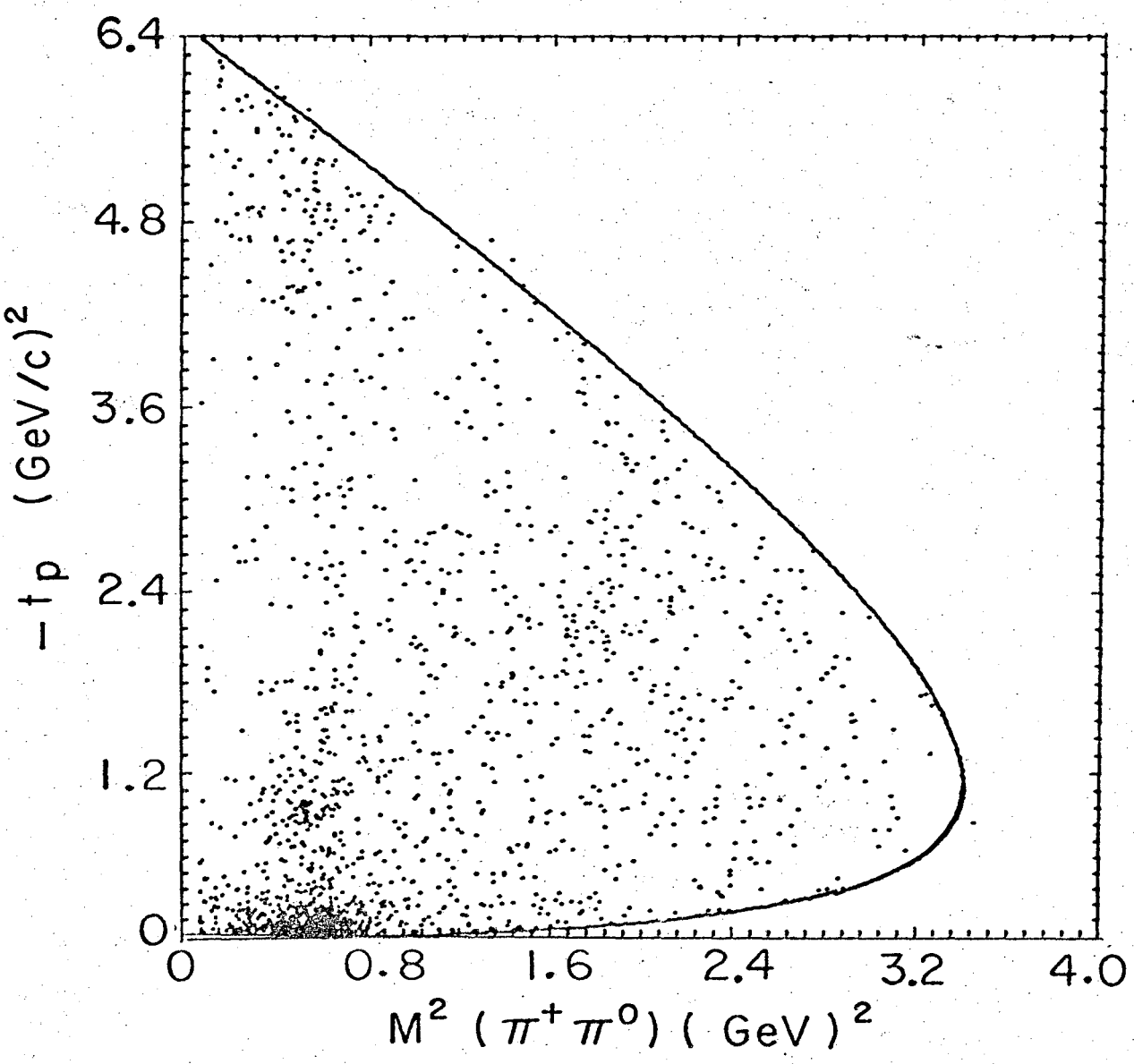

XBL716-3789

Fig. 26

TECHNICAL INFORMATION DIVISION
LAWRENCE BERKELEY LABORATORY
UNIVERSITY OF CALIFORNIA
BERKELEY, CALIFORNIA 94720